A CO SURVEY IN PLANET-FORMING DISKS: CHARACTERIZING THE GAS CONTENT IN THE EPOCH OF PLANET FORMATION

A. S. HALES[1,2], I. DE GREGORIO-MONSALVO[1,3], B. MONTESINOS[4], S. CASASSUS[5], W. F. R. DENT[1,3], C. DOUGADOS[6,7], C. EIROA[8], A. M. HUGHES[9], G. GARAY[5], D. MARDONES[5], F. MÉNARD[6,7], AINA PALAU[10], S. PÉREZ[5], N. PHILLIPS[1,3], J. M. TORRELLES[11], AND D. WILNER[12]

[1] Atacama Large Millimeter/Submillimeter Array, Joint ALMA Observatory, Alonso de Córdova 3107, Vitacura 763-0355 Santiago, Chile; ahales@alma.cl
[2] National Radio Astronomy Observatory, 520 Edgemont Road, Charlottesville, VA 22903–2475, USA
[3] European Southern Observatory, Karl-Schwarzschild-Str. 2, D-85748 Garching bei München, Germany
[4] Department of Astrophysics, Centre for Astrobiology (CAB, CSIC-INTA), ESAC Campus, P.O. Box 78, E-28691 Villanueva de la Cañada, Madrid, Spain
[5] Departamento de Astronomía, Universidad de Chile, Camino El Observatorio 1515, Las Condes, Santiago, Chile
[6] UMI-FCA, CNRS/INSU, France (UMI 3386)
[7] Dept. de Astronomía, Universidad de Chile, Santiago, Chile
[8] Departamento de Física Teórica, Facultad de Ciencias, Universidad Autónoma de Madrid, Cantoblanco, E-28049 Madrid, Spain
[9] Department of Astronomy, University of California, Berkeley, CA 94720, USA
[10] Institut de Ciéncies de l'Espai (CSIC-IEEC), Campus UAB-Facultat de Ciéncies, Torre C5-parell 2, E-08193 Bellaterra, Catalunya, Spain
[11] Institut de Ciéncies de l'Espai (CSIC-IEEC) and Institut de Ciéncies del Cosmos (UB-IEEC), Martí i Franqués 1, E-08028 Barcelona, Spain
[12] Harvard-Smithsonian Center for Astrophysics, Cambridge, MA 02138, USA

ABSTRACT

We carried out a ^{12}CO(3–2) survey of 52 southern stars with a wide range of IR excesses (L_{IR}/L_*) using the single-dish telescopes APEX and ASTE. The main aims were (1) to characterize the evolution of molecular gas in circumstellar disks using L_{IR}/L_* values as a proxy of disk dust evolution, and (2) to identify new gas-rich disk systems suitable for detailed study with ALMA. About 60% of the sample (31 systems) have $L_{IR}/L_* > 0.01$, typical of T Tauri or Herbig AeBe stars, and the rest (21 systems) have $L_{IR}/L_* < 0.01$, typical of debris disks. We detect CO(3–2) emission from 20 systems, and 18 (90%) of these have $L_{IR}/L_* > 0.01$. However, the spectra of only four of the newly detected systems appear free of contamination from background or foreground emission from molecular clouds. These include the early-type stars HD 104237 (A4/5V, 116 pc) and HD 98922 (A2 III, 507 pc, as determined in this work), where our observations reveal the presence of CO-rich circumstellar disks for the first time. Of the other detected sources, many could harbor gaseous circumstellar disks, but our data are inconclusive. For these two newly discovered gas-rich disks, we present radiative transfer models that simultaneously reproduce their spectral energy distributions and the ^{12}CO(3–2) line profiles. For both of these systems, the data are fit well by geometrically flat disks, placing them in the small class of non-flaring disks with significant molecular gas reservoirs.

Key words: circumstellar matter – planetary systems – protoplanetary disks

Online-only material: color figure

1. INTRODUCTION

Most stars are born surrounded by massive circumstellar disks of dust and gas ($M_{disk} \sim 10^{-3}$–10^{-1} $M_\odot$; Williams & Cieza 2011). As the systems evolve, the disks fade, and most of the circumstellar material is accreted either into the central star, into kilometer-size bodies, or dissipated by other gas dispersal mechanisms (Hollenbach et al. 2000; Alexander 2013). Models predict that most of the gas dissipates quickly after the star is formed ($t < 10$ Myr; Boss 2001), while the combined effects of collisional grinding of large bodies together with gravitational resonances can maintain a significant dust grain population for several Myr ($t < 1$ Gyr; Wyatt 2008). The fraction of stellar flux re-radiated by the dust (the disk-to-star bolometric luminosity ratio, L_{IR}/L_*, also referred to as the infrared excess) is a function of the dust mass present in the disk. $L_{IR}/L_* > 10^{-1}$ in young T Tauri and Herbig Ae/Be (HAeBe) stars with massive circumstellar disks, while in more evolved debris disk systems $L_{IR}/L_* < 10^{-3}$ (Zuckerman 2001). Observations indicate that warm ($T > 100$ K) dust located in the disk inner regions ($r < 10$ AU) decays with time as t^{-1} (Rieke et al. 2005; Meyer et al. 2007), as expected from steady-state collisional evolution

models of the dust particles (i.e., the observed dust is secondary; Wyatt et al. 2007), although there are individual systems with luminosities in excess of steady-state predictions (e.g., eta Corvi; Wyatt et al. 2005).

The gas content of protoplanetary disks is more difficult to probe than dust. The zero dipole moment of the most abundant gaseous molecule, H_2, hampers its observation. The second most abundant molecule, carbon monoxide (CO), has a large dipole moment but its observation in circumstellar disks is very often contaminated by large-scale emission, particularly when observed at low angular resolution (Dent et al. 2005; van Kempen et al. 2007). This is unfortunate, as the gas dominates the disk dynamics in the early protoplanetary stages. The gas-to-dust ratio affects the thermal and chemical balance (Jonkheid et al. 2007; Woitke et al. 2009), as well as the dynamic coupling of gas and dust (Weidenschilling 1977; Takeuchi & Artymowicz 2001). The gas temperature determines the scale height of the disk (D'Alessio et al. 1999, 2006), and most importantly, the mechanisms of gas dispersal will set the timescales for the formation of gas-giant planets (Armitage 2011). Consequently, in the field of planet formation, much effort is currently aimed at constraining the timescales over which most

circumstellar gas dissipates (e.g., Carmona 2010; Ingleby et al. 2011; Williams & Cieza 2011).

Dynamical instability models predict the formation of giant planets on orbital timescales ($t \ll 1$ Myr; Boss 2005), while core accretion models require at least a few Myr to form Jovian planets (Pollack et al. 1996). These ages are similar to the age of most T Tauri and HAeBe systems. Large amounts of molecular and atomic gas emission are indeed detected toward such objects (Dutrey et al. 1996; Dunkin et al. 1997; Thi et al. 2001), but these signatures disappear toward systems with lower L_{IR}/L_* values (Zuckerman et al. 1995; Dent et al. 2005; Moór et al. 2011). Dent et al. (2005) carried out a submillimeter survey for CO emission in a sample of 59 objects with a variety of L_{IR}/L_* values, classified as either T Tauri and HAeBe stars or more evolved debris disk-like systems. They found that CO detections are common in objects with $L_{IR}/L_* > 0.01$, but rare in objects with smaller values (<10% of these objects). Optical searches for atomic gas over samples with a wide range of L_{IR}/L_* also indicate that atomic emission lines originating close to the stars disappear in stars with $L_{IR}/L_* < 0.01$ (Dunkin et al. 1997; Redfield et al. 2007), suggesting a possible transition from a gas-rich to a gas-depleted disk near $L_{IR}/L_* \sim 0.01$. However, less than 5% of known HAeBe and debris disk-like systems have been surveyed for gas in either CO or optical emission lines (Thé et al. 1994; Rhee et al. 2007b), hampering robust statistical conclusions.

A few $L_{IR}/L_* \sim 10^{-3}$–10^{-4} systems still show signatures of circumstellar gas, either in the form of CO emission-line profiles associated with orbiting gas (Zuckerman et al. 1995; Dent et al. 2005; Pascucci et al. 2006; Moór et al. 2011) or by showing sharp optical absorption features at the core of photospheric lines, attributable to circumstellar gas around these stars, in the form of shells, clumps, or possibly edge-on disks (Dunkin et al. 1997; Redfield et al. 2007). These systems have become of great interest, as they are thought to be objects transitioning between their protoplanetary and debris disk phases, close to the end of planet formation. Hughes et al. (2008a) conducted submillimeter observations of one of these systems, the A1V star 49 Cet, which revealed a CO gas disk with a depleted inner region, similar to the structures predicted by planetary formation and photo-evaporation models (Armitage 2011; Owen et al. 2012). Another interesting 49 Ceti-like system is HD 21997 (Moór et al. 2011), for which Kóspál et al. (2013) recently obtained ALMA observations. The origin of the gas observed in these systems is still a matter of debate, as it is not yet clear whether it is primordial (left from the protoplanetary phase) or secondary (created by collisions and/or photodesorption from dust grains, e.g., Zagorovsky et al. 2010).

In this work we present a survey for ^{12}CO ($J = 3$–2) gas over a sample of 52 southern stars with circumstellar dust excesses selected from the literature (Thé et al. 1994; Malfait et al. 1998; Mannings & Barlow 1998; Silverstone 2000), using the Atacama Pathfinder Experiment (APEX) and Atacama Submillimeter Telescope Experiment (ASTE) submillimeter telescopes. These two telescopes were the best southern facilities to provide bona fide disk detections in the pre-ALMA era, despite a lack of high spatial resolution and sensitivity. By targeting stars with a range of $L_{IR}/L_\star$, we aim to study the dependence between L_{IR}/L_* and the detectability of CO. No systematic southern surveys for CO gas in protoplanetary disks have been carried out to date. Nyman et al. (1992) used SEST to observe bright southern *IRAS* sources, most of which were evolved objects, such as asymptotic giant branch (AGB), post-AGB, and carbon stars. Recently,

Moór et al. (2011) conducted a CO search over a sample of 20 southern debris disks systems, leading to the detection of the gas-rich debris disk system HD 21997, similar to 49 Cet. A southern survey is necessary, not only to complement results from northern CO surveys (Zuckerman et al. 1995; Greaves et al. 2000; Dent et al. 2005; Liu et al. 2011), but also to provide a sample of gas-rich southern protoplanetary disks that can be targeted for high-resolution studies with ALMA. Follow-up high-resolution, high-sensitivity ALMA observations of other gas tracers can be used to constrain the physico-chemical structure of the newly discovered disks, as well as to test model predictions in which certain molecular species will be subject to significant radial gradients and differentiation (e.g., Walsh et al. 2010).

In Section 2, we present our target selection. Section 3 describes our observations and data reduction. Our main results are shown in Section 4. Detailed radiative transfer modeling of two of the CO-rich objects, HD 104237 and HD 98922, is presented in Section 5. In Section 6 we discuss our results, and in Section 7 we conclude. The Appendix presents individual sources with contaminated CO detections.

2. THE SAMPLE

Our target sample consists of 52 protoplanetary and debris disk systems selected from the literature as having infrared excesses due to orbiting dust (Thé et al. 1994; Malfait et al. 1998; Mannings & Barlow 1998; Silverstone 2000; Sylvester & Mannings 2000). The targets were selected in terms of their photospheric emission-line characteristics (presence or absence of H_α, i.e., T Tauri/HAeBe versus debris disk), isolation from molecular clouds and from bright Two Micron All Sky Survey sources, and particularly their L_{IR}/L_* values. Most stars located close to the Galactic plane ($|b| < 5$) were avoided in order to minimize cloud contamination in the off position. We included most southern HAeBe stars from Malfait et al. (1998) and several southern debris disk systems with $L_{IR}/L_* > 10^{-4}$ from the compilation of Silverstone (2000) and Rhee et al. (2007b). The sample is comprised of isolated HAeBe and debris disk systems to study the evolution of the gaseous component of their protoplanetary/debris disks. The sources of our sample were selected based on different ratios of the infrared excess flux to the photospheric flux L_{IR}/L_*, as a proxy of the evolutionary status of the disks. We covered a range of L_{IR}/L_* that varies over several orders of magnitude, ranging from 10^{-5} to close to unity. We did not consider objects younger than 10^6 yr nor embedded objects, to avoid contamination from protostellar envelopes or from molecular cloud material. Thus, with these proposed "naked" disks, we expect to reduce the possibility of CO contamination by their parental clouds. Table 1 lists our targets and their spectral types and distances, as well as their L_{IR}/L_* values.

The L_{IR}/L_* values listed in Table 1 were taken from the literature (Acke & van den Ancker 2004; Meeus et al. 2012) when available, or by fitting blackbodies to published optical, infrared, and submillimeter data from the literature. The observed spectral energy distributions (SEDs) are assumed to be the sum of the model stellar atmosphere SED (SED$_\star$) and a cooler blackbody of a given temperature (SED$_{disk}$), i.e., SED$_{tot}$ = SED$_\star$+SED$_{disk}$. For each star in Table 1, we searched for the model that minimized the chi-squared (χ^2) difference between the modeled SED$_{tot}$ and the observed data points. The search was performed using the variable-metric routine Migrad of the Minuit

Table 1
Target Sample

	Star	R.A. (J2000)	Decl. (J2000)	Sp. Type	Distance (pc)	L_{IR}/L_*	CO Intensity[f] (K km s^{-1})	Disk Group	Reference
1	HD 105	00:05:52.5	−41:45:11.0	G0V	40	5.9×10^{-4}	<0.02[e]	Debris disk	Hillenbrand et al. (2008)
2	HR 10	00:07:18.2	−17:23:13.1	A2IV/V	160	6.6×10^{-7}	<0.09[c]	Debris disk	Possible bogus IRAS identification (Fajardo-Acosta et al. 1998b).
3	HD 377	00:08:25.7	+06:37:00.4	G2V	40	5.8×10^{-4}	<0.09[a]	Debris disk	Hillenbrand et al. (2008)
4	HD 3003	00:32:43.9	−63:01:53.4	A0V	46	1.4×10^{-4}	<0.11[a]	Debris disk	Rhee et al. (2007b)
5	HD 12039	01:57:48.9	−21:54:05.3	G4V	42	2.1×10^{-4}	<0.02[e]	Debris disk	Rhee et al. (2007b)
6	HD 17848	02:49:01.4	−62:48:23.4	A2V	50	3.9×10^{-5}	<0.14[d]	Debris disk	Sylvester & Mannings (2000)
7	HD 21563	03:24:02.3	−69:37:28.5	A4V	182	9.7×10^{-3}	<0.11[d]	Debris disk	Sylvester & Mannings (2000)
8	HD 28001	04:22:05.9	−56:58:59.5	A4V	. . .	5.0×10^{-3}	<0.11[d]	Debris disk	Sylvester & Mannings (2000)
9	HD 32297	05:02:27.4	+07:27:39.6	A0	112	5.4×10^{-3}	<0.05[c]	Debris disk	Rhee et al. (2007b); L_{IR}/L_* from Meeus et al. (2012)
10	HD 36917	05:34:46.9	−05:34:14.5	A0V	460(5)	1.0×10^{-1}	1.1 ± 0.5[e]	HAeBe disk	Malfait et al. (1998)
11	HD 37411	05:38:14.5	−05:25:13.2	B9 V	510(13)	3.9×10^{-1}	0.5 ± 0.25[e]	HAeBe disk	Malfait et al. (1998)
12	HD 37258	05:36:59.2	−06:09:16.3	A2V	510(6)	3.7×10^{-1}	4.8 ± 1.2[b]	HAeBe disk	Malfait et al. (1998)
13	HD 37389	05:38:08.0	−01:45:07.8	A0	210(7)	1.2×10^{-2}	3.1 ± 0.5[b]	HAeBe disk	Coulson et al. (1998)
14	HD 38087	05:43:00.5	−02:18:45.3	B5 V	199	1.9×10^{-2}	4.5 ± 1.1[e]	HAeBe disk	Malfait et al. (1998)
15	HD 39014	05:44:46.3	−65:44:07.9	A7 V	44	5.7×10^{-5}	<0.02[e]	HAeBe disk	Malfait et al. (1998)
16	HD 250550	06:01:59.9	+16:30:56.7	B9	606(8)	1.4	7.9 ± 1.7[c]	HAeBe disk	de Winter et al. (2001)
17	HD 61005	07:35:47.4	−32:12:14.0	G8V	34	6.8×10^{-4}	<0.02[c]	Debris disk	Hillenbrand et al. (2008)
18	HD 85567	09:50:28.5	−60:58:02.9	B2	770(9)	3.3×10^{-1}	1.4 ± 0.4[e]	HAeBe disk	Malfait et al. (1998)
19	HD 95881	11:01:57.6	−71:30:48.3	A1/2III	118(1)	6.2×10^{-2}	<0.02[e]	HAeBe disk	Malfait et al. (1998)
20	HD 97048	11:08:03.3	−77:39:17.4	A0pshe	175	3.9×10^{-1}	1.4 ± 0.4[c]	HAeBe disk	de Winter et al. (2001); L_{IR}/L_* from Meeus et al. (2012)
21	Hen3-600	11:10:27.8	−37:31:52.0	M4Ve	42(2)	6.6×10^{-2}	<0.02[c]	T Tauri disk	Rhee et al. (2007a)
22	HD 98922	11:22:31.6	−53:22:11.4	A2 IIIe	115	6.5×10^{-1}	**0.11 ± 0.03**[e]	HAeBe disk	Malfait et al. (1998)
23	HD 100453	11:33:05.5	−54:19:28.5	A9Ve	111	6.2×10^{-1}	<0.07[b]	HAeBe disk	Malfait et al. (1998); L_{IR}/L_* from Meeus et al. (2012)
24	HD 100546	11:33:25.4	−70:11:41.2	B9Vne	103	5.6×10^{-1}	2.5 ± 0.3[c]	HAeBe disk	Malfait et al. (1998); L_{IR}/L_* from Meeus et al. (2012)
25	HD 101412	11:39:44.4	−60:10:27.7	B9.5V	160(12)	1.5×10^{-1}	<0.07[c]	HAeBe disk	de Winter et al. (2001)
26	HD 104237	12:00:05.0	−78:11:34.5	A4/5V	116	3.2×10^{-1}	**0.11 ± 0.04**[e]	HAeBe disk	Malfait et al. (1998); L_{IR}/L_* from Meeus et al. (2012)
27	HD 109573A	12:36:01.0	−39:52:10.2	A0	67	5.0×10^{-3}	<0.05[b]	Debris disk	Rhee et al. (2007b)
28	HD 110058	12:39:46.1	−49:11:55.5	A0V	100	2.5×10^{-3}	<0.05[c]	Debris disk	Rhee et al. (2007b)
29	HD 113766	13:06:35.8	−46:02:02.0	F4V	131	2.1×10^{-2}	<0.05[c]	Debris disk	Rhee et al. (2007a)
30	PDS 66	13:22:07.5	−69:38:12.1	K1Ve	86(2)	1.3×10^{-1}	<0.09[a]	T Tauri disk	Hillenbrand et al. (2008)
31	HD 124237	14:14:33.6	−61:47:56.3	B5 V	452	1.6×10^{-1}	<0.09[e]	HAeBe disk	Malfait et al. (1998)
32	HD 132947	15:04:56.0	−63:07:52.6	A0	. . .	2.3×10^{-2}	0.26 ± 0.05[b]	HAeBe disk	Malfait et al. (1998)
33	HD 140863	15:48:49.4	−57:37:55.3	A0 III	. . .	5.2×10^{-1}	<0.02[e]	HAeBe disk	Malfait et al. (1998)
34	HD 142527	15:56:41.8	−42:19:23.2	F6IIIe	198	9.8×10^{-1}	1.7 ± 0.7[b]	HAeBe disk	Malfait et al. (1998); L_{IR}/L_* from Meeus et al. (2012)
35	ScoPMS31	16:06:21.9	−19:28:44.5	M0	145(10)	1.2×10^{-1}	<0.02[e]	T Tauri disk	Dahm & Carpenter (2009)
36	HD 144668	16:08:34.2	−39:06:18.3	A7IVe	207	5.1×10^{-1}	7.2 ± 2.0[b]	HAeBe disk	Malfait et al. (1998); L_{IR}/L_* from Meeus et al. (2012)
37	HD 149914	16:38:28.6	−18:13:13.7	B9.5IV	165	1.3×10^{-3}	1.1 ± 0.4[b]	HAeBe disk	Malfait et al. (1998)
38	HD 155448	17:12:58.7	−32:14:33.5	B 9	606	6.0×10^{-2}	**0.11 ± 0.02**[e]	HAeBe disk	Malfait et al. (1998)
39	KK Oph	17:10:08.0	−27:15:18.2	A8Ve	160(4)	2.0	0.6 ± 0.2[a]	HAeBe disk	de Winter et al. (2001); L_{IR}/L_* from Meeus et al. (2012)
40	HD 158352	17:28:49.6	+00:19:50.2	A8Vp	63	1.6×10^{-4}	<0.6[c]	Debris disk	Rhee et al. (2007b); L_{IR}/L_* from Meeus et al. (2012)
41	HD 158643	17:31:24.9	−23:57:45.5	A0V	131	3.8×10^{-2}	<0.09[c]	HAeBe disk	Malfait et al. (1998)
42	sao185668	17:43:55.6	−22:05:44.7	B3	700(7)	1.1×10^{-1}	<0.02[e]	HAeBe disk	Malfait et al. (1998)
43	HR 6629	17:47:53.5	+02:42:26.2	A0V	29	4.0×10^{-5}	<0.09[b]	Debris disk	Fajardo-Acosta et al. (1998a)
44	HR 6723	18:01:45.1	+01:18:18.2	A2Vn	81	5.0×10^{-5}	<0.4[c]	Debris disk	Rieke et al. (2005)
45	VV Ser	18:28:47.8	+00:08:39.9	. . .	260(3)	9.1	0.47 ± 0.08[c]	HAeBe disk	de Winter et al. (2001)
46	RX J1842.9−353	18:42:57.9	−35:32:42.7	K2	130	8.0×10^{-2}	**0.14 ± 0.03**[a]	T Tauri disk	Hillenbrand et al. (2008)

Table 1
(Continued)

	Star	R.A. (J2000)	Decl. (J2000)	Sp. Type	Distance (pc)	L_{IR}/L_*	CO Intensity[f] (K km s^{-1})	Disk Group	Reference
47	HD 172555	18:45:26.9	−64:52:16.5	A7V	29	8.1×10^{-4}	<0.02[e]	Debris disk	Rhee et al. (2007b)
48	RX J1852.3−370	18:52:17.2	−37:00:11.9	K7V	130	1.8×10^{-1}	<0.09[a]	T Tauri disk	Hillenbrand et al. (2008)
49	HD 181327	19:22:58.9	−54:32:16.9	F6V	50	8.7×10^{-4}	<0.02[e]	Debris disk	Rhee et al. (2007b)
50	HD 178253	19:09:28.3	−37:54:16.1	A2V	39	3.9×10^{-5}	0.57 ± 0.1[e]	Debris disk	Sylvester & Mannings (2000)
51	HD 181296	19:22:51.2	−54:25:26.1	A0V	47	2.4×10^{-4}	<0.18[d]	Debris disk	Rhee et al. (2007b)
52	HD 184800	19:38:40.8	−51:00:18.5	A8/9V	...	1.3×10^{-1}	<0.09[b]	Debris disk	Sylvester & Mannings (2000)

Notes. Spectral types are from the Michigan Spectral Catalog and distances are derived from parallax measures listed in the *Hipparcos* catalog; other references for distance are: (1) Acke & van den Ancker (2004), (2) Rhee et al. (2007a), (3) Straižys et al. (1996), (4) Sandell et al. (2011), (5) distance to the Ori OB1 association, e.g., Hamaguchi et al. (2005), (6) Liu et al. (2011), (7) Coulson et al. (1998), (8) Brittain et al. (2007), (9) Vieira et al. (2003), (10) distance to the Upper Scorpius OB association, e.g., de Zeeuw et al. (1999), (11) Kun et al. (2000), (12) Acke et al. (2005), and (13) Wade et al. (2007). The four detections free of CO emission from extended gas associated with ambient molecular cloud material are marked in boldface.
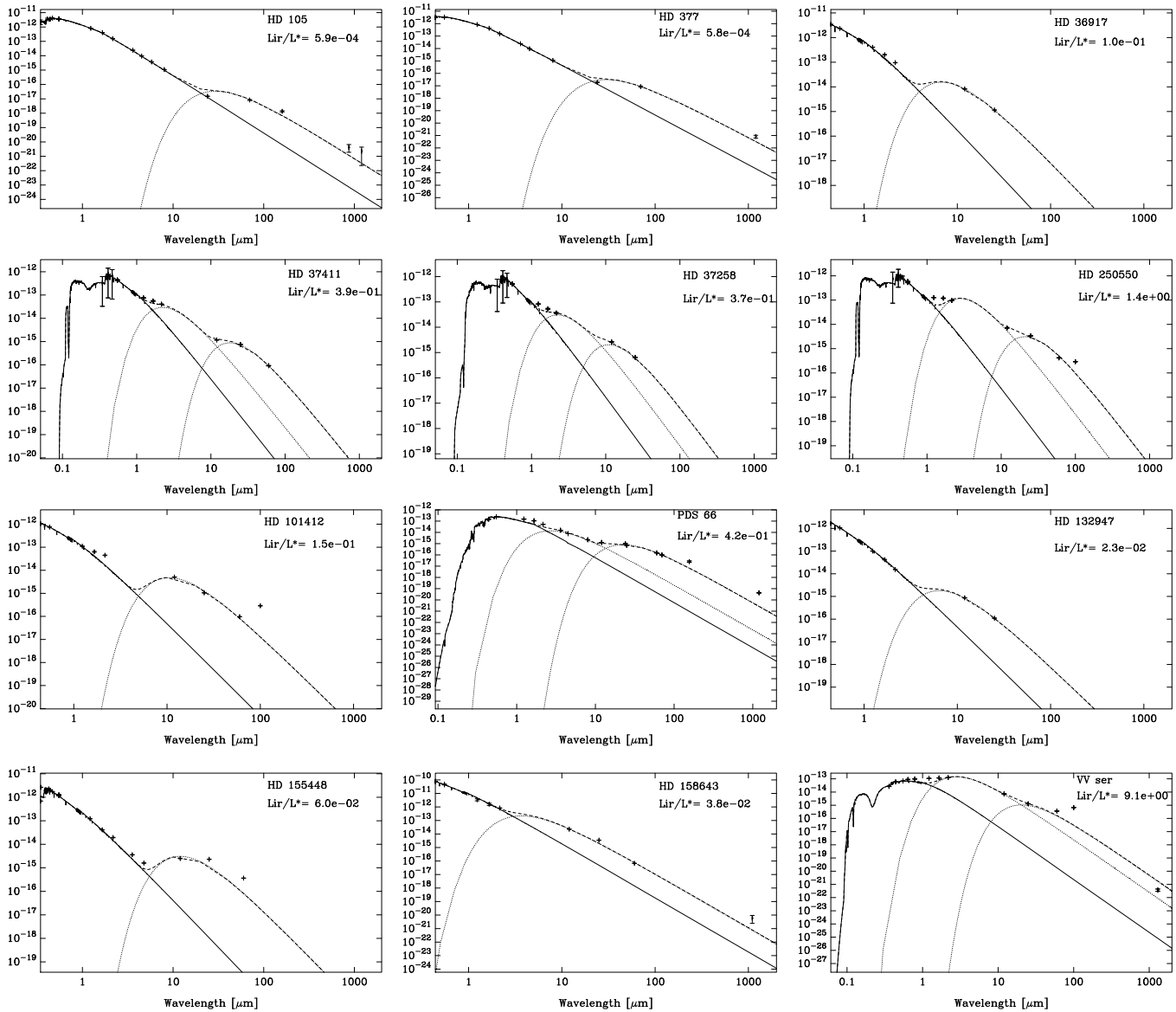[a] ASTE, 2008 June.
[b] APEX, 2008 June.
[c] APEX, 2009 July.
[d] APEX, 2009 December.
[e] ASTE, 2010 July.
[f] Intensity units are in antenna temperatures (T_A^*). Upper limits were computed over a 10 km s^{-1} velocity interval.

Figure 1. Example of our blackbody fit to the available photometry in order to derive L_{IR}/L_* values for stars for which infrared excess were not found in the literature. Units in the vertical axis are in erg cm^{-2} s^{-1}.

package from CERN[13]. The photospheric luminosities (SED$_*$) were computed from stellar model atmospheres (assuming spectral types listed in SIMBAD), which were reddened to match the optical data. A value of $R_V = 3.1$ was assumed. It is well known that the blue and ultraviolet regions of the spectrum are the ones most affected by extinction; therefore, when available, ultraviolet spectra obtained with the *International Ultraviolet Explorer* (*IUE*; Boggess et al. 1978) observatory were added to the SED; they were extremely useful in many cases to estimate $E(B - V)$. L_{IR}/L_* was then obtained by fitting blackbody laws to the infrared excess. In some cases, two blackbodies were required in order to fit both the near-IR and far-IR excesses. We estimate our method to be accurate by factors of 2–3 by comparing our L_{IR}/L_* results with stars with values already published in the literature (Sylvester & Mannings 2000; Meeus

et al. 2012). Example results from our SED fitting method are shown in Figure 1.

In our sample, 59.6% of the sources have L_{IR}/L_* values typical of HAeBe and T Tauri stars (>0.01, for which Dent et al. 2005 find a 48% CO detection rate). The other 40.4% of the objects have $L_{IR}/L_* < 0.01$ and have been selected in order to characterize the zone where the gas-rich to gas-depleted disk transition is thought to occur ($L_{IR}/L_* \sim 0.01$; Dent et al. 2005). The Herbig Ae star HD 100546, known to harbor a CO-rich protoplanetary disk, was also included in the sample as a control target (Panić et al. 2010).

3. OBSERVATIONS AND DATA REDUCTION

Here we describe the main ^{12}CO(3–2) single-dish survey and complementary far-infrared and submillimeter line and continuum observations of a few of the detected sources.

3.1. ASTE and APEX $^{12}CO(3–2)$ Observations

Observations were carried out using ASTE (Kohno [2005]) and APEX[14] (Güsten et al. [2006]), both located at 5000 m above sea level in the Atacama Desert. Spectra toward each star were acquired using the standard on–off observing pattern to remove atmospheric continuum emission, using typical beam-switching offsets of 180 arcsec in azimuth. In cases where spurious absorption lines were seen in the spectra due to ambient emission in the off position, a second observation using an off position of −180 arcsec in azimuth was obtained. Spectral line observations of the $J = 3–2$ transition of ^{12}CO (rest frequency $\nu = 345.795991$ GHz) were made using the 2-SB 350 GHz receiver on ASTE and the SHeFI 345 GHz receiver on APEX. The velocity resolution on ASTE and APEX was 0.5 km s^{-1} and 0.4 km s^{-1}, respectively. The total bandwidths covering the ^{12}CO line were 1 GHz and 0.5 GHz for APEX and ASTE, respectively. The beam widths of APEX and ASTE at this frequency were 18 and 21 arcsec, respectively. Typical disk sizes for protoplanetary disks are a few hundred AU, and will therefore be unresolved in our observations. The corresponding main beam efficiencies (η_{mb}) listed on the ASTE[15] and APEX[16] instrument Web sites are 0.6 and 0.73.

In order to reach a targeted rms noise level of 0.02–0.04 K (comparable to the northern survey of Dent et al. [2005]), typical integration times of 1 and 2 hr were required for APEX and ASTE, respectively. The survey was completed in different observing blocks during 2008 June, 2009 July, 2009 December, and 2010 July (APEX Project Codes C-081.F-0010B, C-083.F-0187A, and C-084.F-0478A). The precipitable water vapor was typically between 1 mm and 2 mm, with exceptionally good conditions (0.3–0.9 mm) encountered during the 2010 July run. Close to 80 hr of telescope time were required to complete the survey.

The ASTE spectra were converted to FITS format using the Newstar package.[17] After conversion to FITS, both the ASTE and APEX spectra were processed using the GILDAS/CLASS reduction software (Guilloteau & Lucas [2000]).[18] The individual raw data scans were visually inspected for identifying spikes, outliers, and baselines instabilities. Scans with problems were excluded from the data reduction. A baseline substraction from each individual scan was performed, excluding channels that showed spectral emission line. A polymonial of degree three or less was used for the baseline fitting. In order to produce final spectra with the highest signal-to-noise ratio (S/N), the scans were averaged. The rms noise was computed in the averaged spectra, excluding the channels that contained a signal from the object of interest.

The 2008 ASTE data were affected by an instrumental 1 MHz sinusoidal ripple of variable amplitude and phase. This artifact was removed from each individual 10 s integration by fitting the first peak of the spectrum's Fourier components and subtracting it (see Hughes et al. [2010], for details).

3.2. LABOCA Archive Observations

An 870μm continuum map of the HD 104237 system obtained with the LABOCA bolometer array camera on APEX (Siringo et al. [2009]) was retrieved from the ESO archive[19] (PI: R. Liseau, project code 082.F-9304A). The observations were performed on 2008 December 28 in stable conditions with a line of sight $\tau = 0.38$, using a standard compact spiral raster that yields excellent spatial sampling. The instrumental sensitivity, as determined by flux calibrator measurements, was reduced to approximately 64% of normal this night due to a bias problem. The data were scaled to compensate for this in the reduction, but the noise is accordingly increased.

Data were reduced using a custom pipeline in BoA package 7.[20] The pre-processing steps consisted of flagging dead or cross-talking channels and frames with too high telescope accelerations and unsuitable mapping speed, as well as temperature drift correction using two blind bolometers. The data reduction process included flat-fielding, opacity correction, calibration, correlated noise removal (atmospherics fluctuations seen by the whole array, as well as electronic noise originated in groups of detector channels), and de-spiking. Every scan was visually inspected to identify and discard corrupted data. The final map shows an angular resolution of 19″ and an rms noise of 18 mJy/beam (calculated in the central part of the map).

3.3. Herschel/PACS Archive Observations

We have analyzed unpublished *Herschel* observations of HD 98922 using the PACS instrument in both photometric and spectroscopic modes that exist in the *Herschel* Science Archive (Pointed Range Spectroscopy observing mode). We used the Level 2 archived standard products produced by the *Herschel* Standard Product Generation software, version 10.3.0. PACS photometry was extracted by point spread function fitting to obtain 70 and 160 μm fluxes (3815.2 and 877.5 Jy, respectively). The rms in the 70 and 160 μm maps are 0.2 and 0.4 mJy pixel^{-1}, respectively. The uncertainty in the derived fluxes will be dominated by the 5% absolute calibration accuracy of PACS (Balog et al. [2013]), so we quote 5% photometric errors for the PACS final fluxes in Table [4].
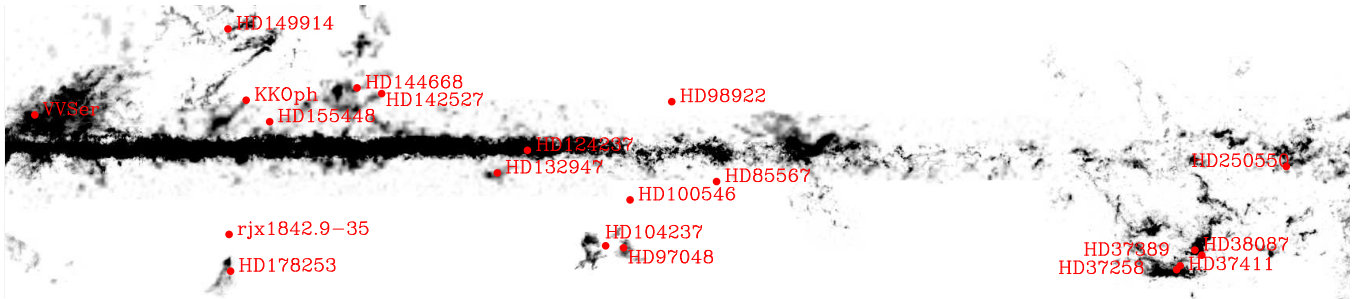
4. RESULTS

Figure [2] shows the distribution of our detected targets against known molecular clouds. Figure [3] shows the spectra for four detections that appear to be free from foreground/background contamination in the off spectra. Association of the CO emission with the targeted stars may be determined by comparing the velocity of the detected emission to the velocity of the star, determined from optical spectra (the known V_{LSR} velocity of the stars are plotted on top of the spectra, when available).

Integrated line intensities on the detections, or 1σ upper limits, are presented in Table [1] in antenna temperature units. Upper limits were computed as $T_{rms}\Delta v \sqrt{N}$, where T_{rms} is the noise measured in the spectra, Δv is the velocity resolution of each channel, and N is the number of channels over a 10 km s^{-1} velocity interval. We report an integrated CO intensity of 2.5 ± 0.3 K km s^{-1} ($T_A^\star$) toward our control target HD 100546, compared to the previously measured 2.9 ± 0.4 K km s^{-1}, which are consistent within the uncertainties (also in $T_A^\star$; Panić et al. [2010]).

---

[14] Based on observations with the Atacama Pathfinder EXperiment (APEX) telescope. APEX is a collaboration between the Max Planck Institute for Radio Astronomy, the European Southern Observatory, and the Onsala Space Observatory.
[15] http://www.nro.nao.ac.jp/~aste/cfp2011/note.html
[16] http://www.apex-telescope.org/telescope/efficiency/
[17] http://www.nro.nao.ac.jp/~nro45mrt/obs/newstar/
[18] http://www.iram.fr/IRAMFR/GILDAS/doc/html/class-html/class.html

[19] http://archive.eso.org
[20] http://www.apex-telescope.org/bolometer/laboca/boa/

Figure 2. Location of southern HAeBe with CO(3–2) detections shown against known molecular cloud CO maps (from Milky Way CO; Dame et al. 2001).
(A color version of this figure is available in the online journal.)

A single-dish non-detection of CO implies that neither a CO disk nor CO ambient emission is detected toward the targeted star (a fainter CO disk could be present below the sensitivity limit).

However, a CO detection does not necessarily mean that a gaseous disk is present. van Kempen et al. (2007) already noted the difficulty of disentangling ambient CO emission versus protoplanetary disk signatures when looking for circumstellar CO using a single-dish telescopes toward pre-main-sequence stars in Lupus. While most debris disk systems are isolated from molecular clouds, younger stars are usually still associated with their parent clouds (see Figure 2), increasing the probability of contamination from ambient CO in the spectra (either in the off or on position, or both), and interferometric observations are needed to filter out the extended cloud emission.

We surveyed 52 stars for ^{12}CO(3–2) emission and obtained detections toward 20 objects. Of the detected sources, 18 (90%) have $L_{IR}/L_* > 0.01$. This trend is in agreement with the findings of the survey from Dent et al. (2005) in which ~50% of the systems with $L_{IR}/L_* > 0.01$ have significant CO detections. Our statistics are, however, biased due to cloud contamination toward many of the sources. A description of the individual sources and results with detections with background/foreground contamination is given in the Appendix.

4.1. ^{12}CO Disk Detections

4.1.1. HD 104237

HD 104237 (DX Cha) is the only early-type star of the young ϵ Cha cluster (3–5 Myr; Feigelson et al. 2003). It is a Herbig Ae star (A4Ve-A8Ve; Grady et al. 2004; Lyo et al. 2008) with infrared excess (Walker & Wolstencroft 1988; Hu et al. 1989). At least five stars are found within 15 arcsec of HD 104237, labeled with letters from "B" to "E" (Feigelson et al. 2003). They are lower-mass stars, of which at least two have IR excesses and emission lines, associated with T Tauri type stars (Grady et al. 2004). Optical spectroscopy has revealed that HD 104237 is actually a close binary system, where the secondary is a K3 star (HD 104237−2) at ~0.2 AU (Böhm et al. 2004). Model fits to its SED suggest that HD 104237 is surrounded by a dust disk with an irradiated inner wall that shadows the outer disk (Meeus et al. 2001). Very Large Telescope (VLT) AMBER observations resolve the inner radius of the ring at $R \sim 0.45$ AU (Tatulli et al. 2007; Garcia et al. 2013). The binary separation $a = 0.22$ AU implies the disk is circumbinary (Böhm et al. 2004).

HD 104237 belongs to a small group of SED-predicted flat disk sources that exhibit moderate [O I] emission at optical wavelengths (Acke et al. 2005). Recent modeling of the optical to mid-infrared SED by Fang et al. (2013) supports the Meeus et al. (2001) SED interpretation of HD 104237 being surrounded

by a self-shadowed (i.e., non-flared) dust disk (therefore being a Group II source, according to the classification of Meeus et al. 2001).

There is evidence of circumstellar gas around HD 104237 detected in the Brγ line (Kraus et al. 2008), and marginally detected in the optical [O I] 6300 Å line (the detection is contaminated by photospheric absorption; Acke et al. 2005). While [O I] emission could arise from warm surface layers of an orbiting gas disk, the hydrogen Brγ emission appears to come from a gaseous inner (<1 AU) disk (Kraus et al. 2008). Garcia et al. (2013) suggest, from recent VLT data, that Brγ is actually very compact and mostly arises from the close environment of each component of the binary, probably related to accretion flows. However, these findings are derived from interferometric observations that filter out any component extended over scales larger than a few AU. No H$_2$ emission was detected in the pure rotational line in the mid-IR (Carmona et al. 2008). Meeus et al. (2012) detected strong [O I] 63.2 μm emission toward HD 104237 using PACS on the *Herschel Space Telescope*, indicating that there are significant amounts of circumstellar gas around this system. A large-scale jet elongated in the southeast–northwest directions and seen in Lyα originates from this source (Grady et al. 2004).

A double-peaked CO line profile is detected in the ASTE spectrum (Figure 3), centered at 5 km s^{-1} and of roughly 8–9 km s^{-1} width. HD 104237 is located in a region between the Cha II and Cha I clouds, at the edge of Cha II. The NANTEN ^{12}CO(1–0) map (Mizuno et al. 2001) shows ambient emission close to the HD 104237 system in the 2–6 km s^{-1} range. The stellar velocity plotted on top of the spectrum was obtained from Gontcharov (2007). The CO emission is centered at the star's position (confirmed by spectra with different off positions), indicating that the disk contribution dominates the ambient cloud contribution.

4.1.2. HD 98922

Together with HD 104237, HD 98922 is also a member of the small group of flat-disk sources with [O I] emission at optical wavelengths (Acke et al. 2005). No H$_2$ emission was detected in the pure rotational line in the mid-IR (Martin-Zaïdi et al. 2008). Similar to HD 104237, the 63.2 μm [O I] line is also detected (Fedele et al. 2013).

A single-peaked profile is detected in CO(3–2) toward HD 98922 (Figure 3), centered at −7 km s^{-1}. The line velocity is offset by 15 km s^{-1} from the radial velocity listed in Acke et al. (2005). This offset is, however, comparable to their centroiding error in the stellar velocity determination (between 8 and −15 km s^{-1}). HD 98922 is located 7° above the Galactic plane ((l, b) = (289.78, +07.21)) in the direction of the third
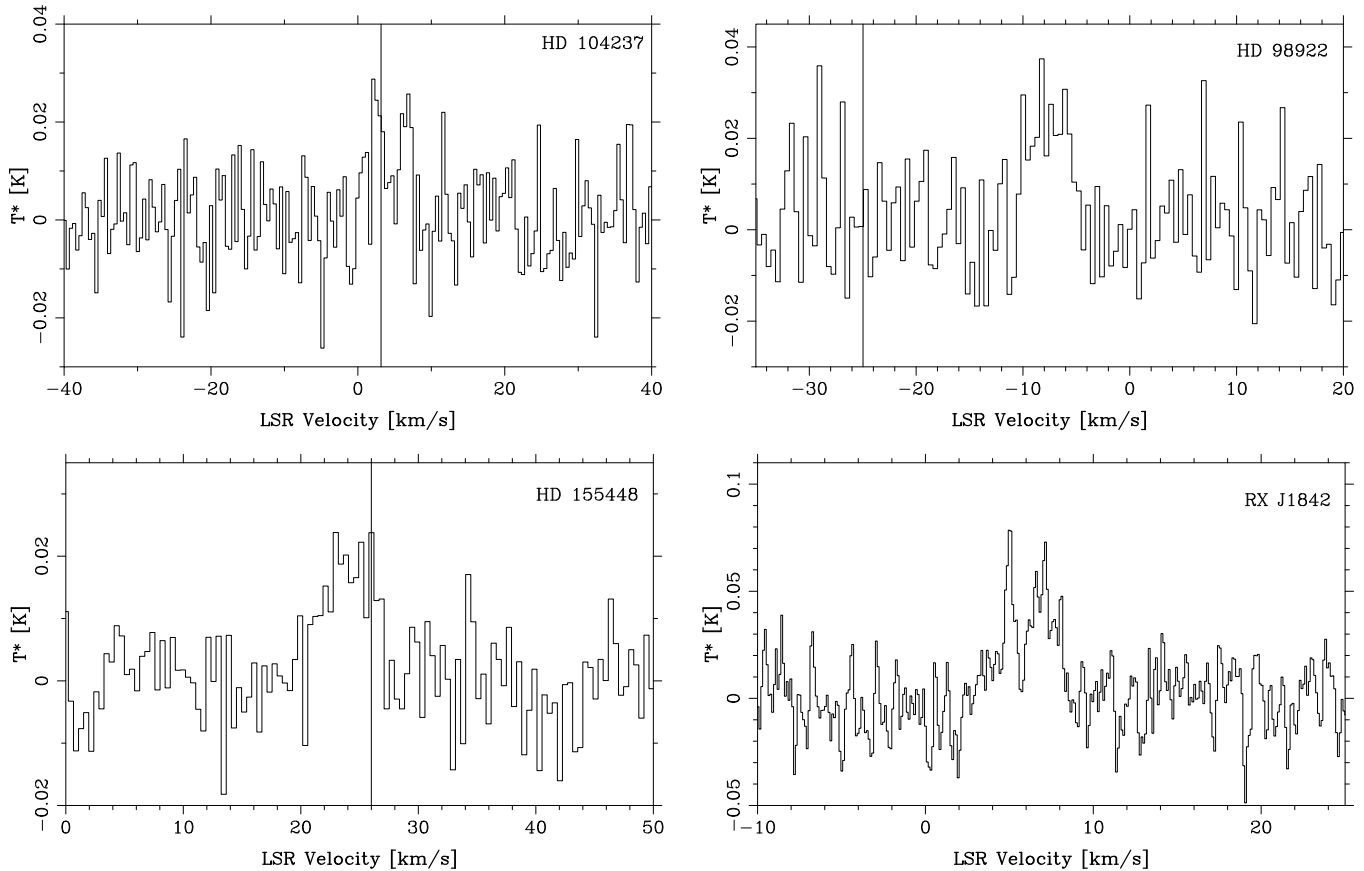
Figure 3. ASTE spectra for the four new CO disk detections. When available, the stellar velocity has been plotted with a vertical line (in V_{lsr}). Intensity units are in antenna temperature (T_A^*).

quadrant (Dame et al. 2001), but there are no prominent known molecular clouds on the line of sight. The two closest clouds derived from extinction maps are located at $(l, b) = (290.70, 5.83)$ and (290.93, 7.50), respectively (Dobashi et al. 2005). Since there are no known molecular clouds in the line of sight, nor evidence of contamination in the reference spectrum, we associate the CO emission with the stellar position (within the ASTE primary beam).

4.1.3. HD 155448

Classified as a B9-type star, there have been two main interpretations in the literature concerning the nature of HD 155448: it has been proposed to be a HAeBe star with a circumstellar disk (Malfait et al. 1998; Schütz et al. 2004), or a post-AGB star surrounded by an ejected shell (Luna et al. 2008; Ortiz et al. 2005).

Schütz et al. (2011) seem to have resolved this dichotomy by analyzing the system in detail using resolved photometry and spectroscopy. They propose that this is actually a quintuple system and rule out a possible post-AGB nature: four out of five components lie close to the zero-age main sequence in the HR diagram. According to Schütz et al. (2011), the C component presents spectral signatures corresponding to a star with a circumstellar disk.

A single-peaked profile is detected toward HD 155448, centered at 24 km s^{-1} and of roughly 6 km s^{-1} width (Figure 3). Luna et al. (2008) detected optical absorption features of H$_\alpha$ and carbon at 36 km s^{-1} and 26 km s^{-1}, respectively, which they associated with an expanding circumstellar envelope. Even though the expanding post-AGB envelope scenario has been

ruled out by Schütz et al. (2011), it is interesting to note that the ^{12}CO(3–2) emission of HD 155448 coincides in velocity with the optical atomic carbon emission detected in Luna et al. (2008).

4.1.4. RX J1842.9−353

A double-peaked profile characteristic of rotating disks is detected toward RX J1842.9−353 in the ASTE spectrum (Figure 3). The ASTE detection was analyzed alongside complementary submillimeter array (SMA) data presented in Hughes et al. (2010). In the SMA data, the dust disk was detected and marginally spatially resolved, while the CO observations resulted in an interferometric upper limit.

4.2. LABOCA 870 μm Continuum Map of HD 104237

The LABOCA 870 μm continuum map of HD 104237 (Figure 4) shows a clear detection of the primary disk, but also significant extension to the southeast, consistent with emission from a disk around the D or E components in the system. Based on the mid-IR detection of a disk around the E component by Grady et al. (2004), we have extracted fluxes using a model of two point sources separated by the 14″9 A–E separation vector (Figure 5). This yielded fluxes of 154 ± 24 mJy and 91 ± 24 mJy for the A and E components, respectively (uncertainties allow for S/N, calibration uncertainty, and anti-correlated error of the two fluxes), and a position offset error of under 2″. Due to the system configuration, any flux from the D component will mostly be incorporated in the E component flux, and any
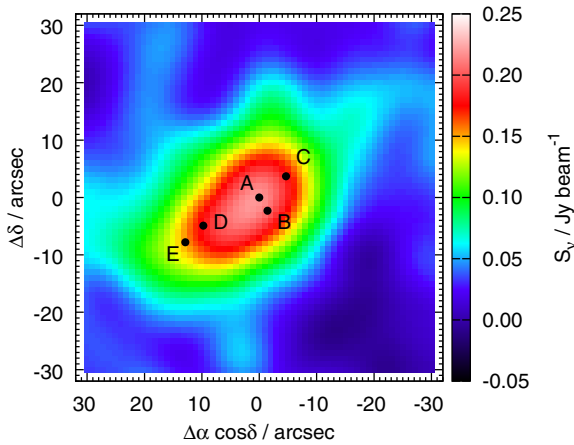
Figure 4. LABOCA map of HD 104237 smoothed with a half-beam Gaussian (FWHM = 9″3), with stellar component positions plotted (component A corresponds to HD 104237).

emission from the B and C components will be included in the A component flux.

5. RADIATIVE TRANSFER MODELING OF HD 104237 AND HD 98922

In this section, we use the three-dimensional radiative transfer Monte Carlo code MCFOST (Pinte et al. 2006) to model simultaneously the SEDs and ^{12}CO(3–2) spectra of two of the four sources exhibiting emission from a disk and not contaminated by known molecular clouds. We model only two sources, HD 104237 and HD 98922. RX J1842.9−353 is already modeled by Hughes et al. (2010), and given the complexity of the HD 155448 system (Schütz et al. 2011), we do not carry out radiative transfer of this system but do include it in our final detection statistics.

The models presented in this section assume that the dust and gas are well coupled, with a dust-to-gas ratio of 10^{-2} and a 10^{-4} CO abundance with respect to H_2. The canonical average dust-to-gas ratio found in the literature for the interstellar medium (ISM) is of the order of 10^{-2}; we assume that young protoplanetary disks should then have similar ratios although decreasing as the gas dissipates and dust grains grow (Birnstiel et al. 2010). The relative abundances of CO and H_2 are constant in the diffuse ISM and equal to 10^{-4} (Federman et al. 1980;

Lee et al. 1996). These standard values for the dust-to-gas and CO/H_2 ratios therefore constitute a first reasonable approach to the true physical properties of the disks.

MCFOST assumes that the gas–dust thermal exchange is perfect and that gas and dust are in local thermodynamic equilibrium (LTE) throughout the disk. The LTE approximation is justified for low-J CO lines, as has been demonstrated several times (Pavlyuchenkov et al. 2007; Panić & Hogerheijde 2009). Freeze out is a natural outcome of a cold media containing dust and gas. It is well known from laboratory and from astronomical data that CO freezes out at ∼20 K (Qi et al. 2011; de Gregorio-Monsalvo et al. 2013). Models accounting for the freeze out of CO into dust grains at a temperature of ∼20 K can also be incorporated in MCFOST.

5.1. HD 104237 SED and CO Disk Modeling with MCFOST

Due to its complexity (circumstellar activity, multiplicity), the basic stellar parameters of HD 104237 have been loosely constrained. There is a large discrepancy in temperature, luminosity of the primary (HD 104237, or HD 104237A hereafter), and the secondary (HD 104237A-2) star (e.g., for the primary $T \sim 7300$–9550 K and $L \sim 20$–60 $L_\odot$; Fumel & Böhm 2012). Table 2 summarizes the available photometric data used for the SED modelling of this system. For our SED fitting we adopted effective temperatures and luminosities from Tatulli et al. (2007), that is, $T_{\mathrm{eff},1} = 8000$ K, $L_1 = 30\ L_\odot$ for the primary and $T_{\mathrm{eff},2} = 4750$ K, $L_2 = 3\ L_\odot$ for the secondary star. This combination of stellar parameters is able to fit the available optical and *IUE* data (Boggess et al. 1978) with no need for any reddening (Figure 6), and was therefore adopted as the energy source for the radiative transfer modeling. Other parameters such as stellar masses and stellar radii are taken from Garcia et al. (2013). The fundamental stellar parameters assumed for modeling the energy input of the system are presented in Table 3.

The surface density distribution of the disk that was adopted is the tapered-edge model (Andrews et al. 2009; Williams & Cieza 2011),

$$\Sigma = \Sigma_C \left(\frac{R}{R_C} \right)^{-\gamma} \exp \left[- \left(\frac{R}{R_C} \right)^{2-\gamma} \right], \qquad (1)$$

where Σ_C is the surface density at the characteristic radius R_C, and γ is a variable physically related to the disk's viscosity (Hughes et al. 2008b). The latter controls the radial variation of
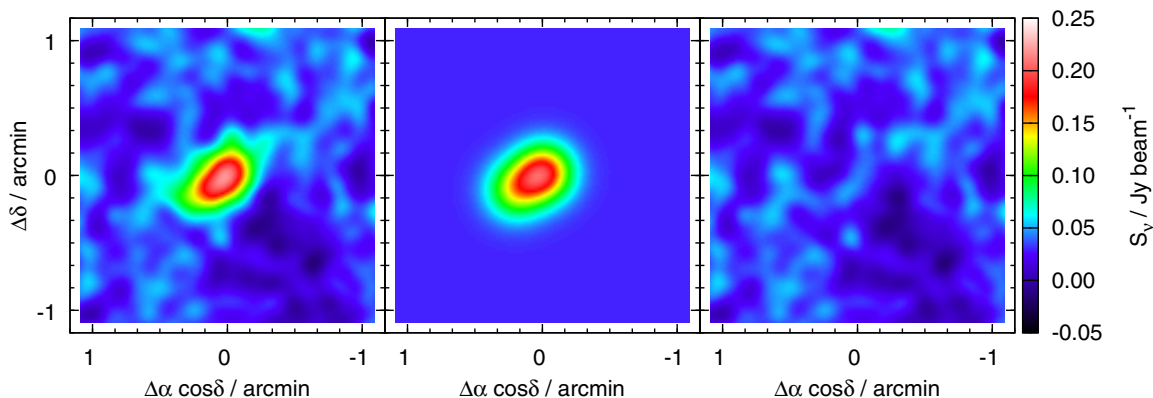
Figure 5. Left: LABOCA map; center: fitted model of two effective beam-sized Gaussians (FWHM = 18.6) with separation of A and E components; Right: maps with the model subtracted.

Table 2
HD 104237 Photometric Data

Wavelength (μm)	Flux (erg/cm^{-2}/s/Å)	Flux Error (erg/cm^{-2}/s/Å)	Reference Filter	Reference
0.345	6.8022E−12	6.8022E−13	u	Hauck & Mermilliod (1998)
0.347	6.9823E−12	6.9823E−13	U	Malfait et al. (1998)
0.411	1.3423E−11	1.3423E−12	v	Hauck & Mermilliod (1998)
0.425	1.2706E−11	1.2706E−12	B	Malfait et al. (1998)
0.440	1.2443E-11	1.6045E−13	B	Høg et al. (2000)
0.467	1.2078E−11	1.2078E−12	b	Hauck & Mermilliod (1998)
0.548	8.5312E−12	8.5312E−13	y	Hauck & Mermilliod (1998)
0.550	8.7983E−12	8.7983E−13	V	Malfait et al. (1998)
0.550	8.3176E−12	7.6609E−14	V	Høg et al. (2000)
0.640	5.1643E−12	5.1643E−13	R	Cutri et al. (2003)
1.215	1.6590E−12	1.6590E−13	J	Malfait et al. (1998)
1.235	1.4818E−12	3.1391E−14	J	Cutri et al. (2003)
1.654	1.0114E−12	1.0114E−13	H	Malfait et al. (1998)
1.662	8.8605E−13	4.8173E−14	H	Cutri et al. (2003)
2.159	6.2851E−13	1.0420E−14	K_s	Cutri et al. (2003)
2.179	7.0558E−13	7.0558E−14	K	Malfait et al. (1998)
3.547	3.9628E−13	3.9628E−14	L	Malfait et al. (1998)
4.769	1.9592E−13	1.9592E−14	M	Malfait et al. (1998)
12.000	3.4073E−14	3.4073E−15	12 μm	Beichman et al. (1988)
25.000	7.8464E−15	7.8464E−16	25 μm	Beichman et al. (1988)
60.000	7.0254E−16	7.0254E−17	60 μm	Beichman et al. (1988)
65.000	7.1214e−16	2.7749e−17	65 μm	Yamamura et al. (2011)
90.000	3.1830e−16	1.1110e−17	90 μm	Yamamura et al. (2011)
100.000	2.4173E−16	2.4173E−17	100 μm	Beichman et al. (1988)
140.000	7.8254e−17	9.1042e−18	140 μm	Yamamura et al. (2011)
160.000	5.3070e−17	1.0004e−17	160 μm	Yamamura et al. (2011)
870.000	1.9570E−19	1.9570E−20	870 μm	This work
1300.000	1.5965E−20	3.5478E−21	1300 μm	Henning et al. (1994)
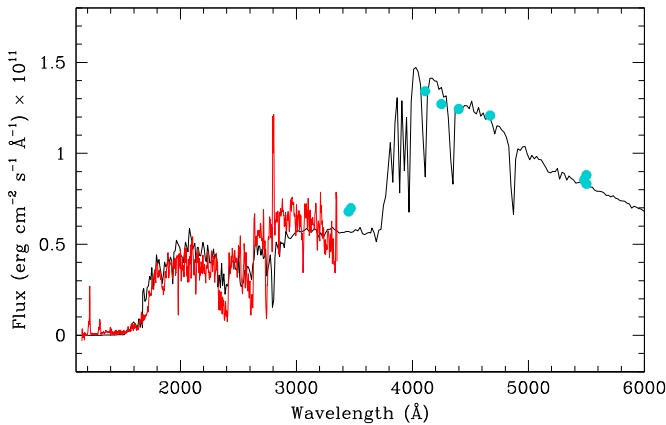
Figure 6. HD 104237 spectral type fit to the *IUE* (red line) and optical data (blue dots). The synthetic spectra (black line) correspond to the sum of two Kurucz models (T_1 = 8000, log(g_1) = 4.0 and T_2 = 4750, log(g_2) = 4.5); (Kurucz 1993), where the second model was scaled such that the integral of the first one divided by the integral of the second one is 10. The combined model has been computed after adding these two files. The combined model has been normalized to the flux at V with no reddening and with $E(B-V) = 0.05$. The best fit does not seem to require any reddening.

the density distribution by providing a power law distribution in the inner disk with an exponential taper in outer regions. The inner rim value of 0.45 AU was adopted from Tatulli et al. (2007). The flaring parameters were also varied, assuming that at a given radius the disk column density is distributed vertically like a Gaussian with a scale height

$$H = H_c R_c \left(\frac{R}{R_C} \right)^{\psi}, \qquad (2)$$

Table 3
HD 104237 Disk Model

Physical Parameter	Value	Reference
Stellar Properties		
Spectral type 1	A4V	Tatulli et al. (2007)
Spectral type 2	K3V	Tatulli et al. (2007)
Primary star mass: M_1 ($M_\odot$)	2.2	Garcia et al. (2013)
Secondary star mass: M_2 ($M_\odot$)	1.4	Garcia et al. (2013)
Effective temperature: T_1 (K)	8000	Tatulli et al. (2007)
Effective temperature: T_2 (K)	4750	Tatulli et al. (2007)
Stellar luminosity: L_1 ($L_\odot$)	30	Tatulli et al. (2007)
Stellar luminosity: L_2 ($L_\odot$)	3	Tatulli et al. (2007)
Distance: d (pc)	115	Tatulli et al. (2007)
Disk Structure		
Disk total mass: M_D ($M_\odot$)	$100 \times M_d$	This work
Disk dust mass M_d ($M_\odot$)	4×10^{-4}	This work
Inner rim: R_{in} (AU)	0.45	Tatulli et al. (2007)
Characteristic radius R_C (AU)	90	This work
Characteristic height h_C (AU)	6	This work
Surface density exponent: γ	0.8	This work
Flaring exponent: ψ	0.0	This work
Inclination angle: i (deg)	31	This work
Systemic velocity: $V_{\rm lsr}$ (km s^{-1})	4.2	This work

where $H_C R_C$ is the scale height at the characteristic radius R_C and ψ describes the dust disk flaring. In summary, the total disk mass (M_D, obtained by integrating the entire density distribution), R_C, γ, ψ, and h_C (the scale height at the characteristic radius) were variables of the model fitting routine.

The dust grains consist of astronomical silicates and are distributed in size following a power law, $n(a) \propto a^{-3.6}$, between
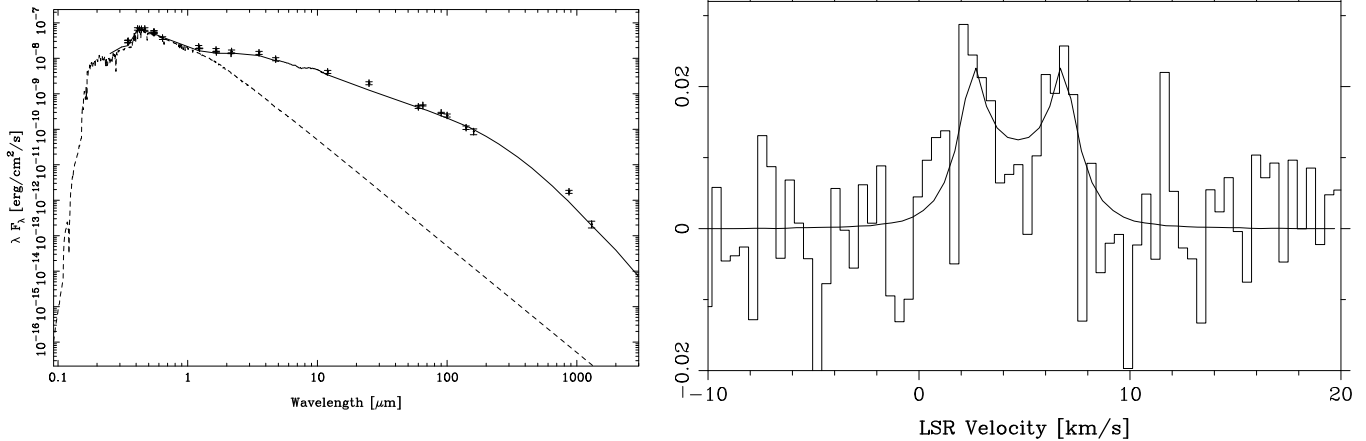
Figure 7. Left: observed SED of HD 104237 (black points with error bars) plotted against the MCFOST disk model that fits the optical to submillimeter data (solid line). Right: the MCFOST CO model of HD 104237 (solid line) fits well the ASTE submillimeter data. Intensity units are in antenna temperature (T_A^*).

$a_{\min} = 0.03\,\mu m$ and $a_{\max} = 7000\,\mu m$ (Draine & Lee 1984). Without constraints on the disk sizes (i.e., direct imaging), the fitting process is a highly degenerate problem: changes in the disk outer radius and the surface density distribution can be made to artificially match the SED and CO data. A range of γ values from 0 to 2 was explored in order to fit the SED data until a good match was found. A range in disk outer radii from 60 to 120 AU was explored. The disk's total mass was mostly constrained by the long wavelength data points. However, given the uncertainties and assumptions in the models, we did not attempt to optimize these fits any further and therefore no formal errors are quoted in the variable terms. We stress the fact that this model is simply a rough model that matches the data and is by no means a best-fit model in formal terms.

The SED can be fit with a 90 AU disk of total dust mass $4 \times 10^{-4}\,M_\odot$. The extension of the fitted disk is comparable with the 70 AU disk radius estimated by Grady et al. (2004). The total mass we derive is in agreement with that of Henning et al. (1994), who estimated the mass of the system based on the 1.3 mm data. Fang et al. (2013) estimate smaller disk masses in their models, but with a smaller wavelength range ($<20\,\mu m$), their SED fits were not sensitive to larger dust grains. No flaring is required to match the SED ($\psi = 0$), in good agreement with previous SED studies of the disk's vertical structure, which indicate the disk is not flared (Meeus et al. 2001; Fang et al. 2013). We use this fiducial model to attempt to also reproduce the CO observations.

The degeneracies when mining pure SED modeling lacking resolved images are well known, but nonetheless the SED information and the kinematic information from the gas lines can be used to further constrain the disk geometry (Dent et al. 2005; Panić & Hogerheijde 2009; Hughes et al. 2010). MCFOST uses the radiation and temperature fields (assuming $T_{\text{dust}} = T_{\text{gas}}$) to compute the level populations of CO (assuming LTE) and to produce line emission surface brightness profiles. We have used a gas-to-dust ratio of 100:1 and an abundance of CO of 10^{-4} respective to H_2, constant throughout the disk.

Grady et al. (2004) estimate a disk inclination angle of 18^{+14}_{-11} degrees. This value was used as initial estimate, but was then allowed to vary during the different runs. The velocity field is that of Keplerian rotation with a central object of mass equal to that of the combined binary system ($M_1 + M_2 = 3.6\,M_\odot$). The systemic velocity (V_{lsr}) and the inclination of the disk were varied until a good match was found.

We find that the standard model over predicts the flux densities by a factor of 2.5. As discussed in Hughes et al. (2010), there are several ways of reducing the predicted CO intensities without changing the dust distribution. Different CO/H_2 ratios, dust-to-gas ratios, or different gas temperatures would significantly change the observed intensities. By incorporating the freeze out of CO molecules into dust grains at temperatures below 20 K (that is, the abundance of CO drops to zero where $T < 20$ K in the disk), the model images fit the data without needing to change either the global abundance of CO/H_2, or the disk total mass. The parameters that reproduce the CO data (Figure 7) are listed in Table 3.

5.2. HD 98922 SED and CO Disk Modeling with MCFOST

Contrary to HD 104237, very little information is available on HD 98922. Together with HD 104237, it is one of the few close-by, southern, flat disks with signs of a rich gas chemistry.

The determination of the parameters for HD 98922 turned out to be a particularly difficult issue. The star is bright ($V \sim 6.8$) and was classified as a B9 Ve (Houk 1978). Taking the typical absolute magnitude for a B9 V star, $M_V = +0.2$, would imply a distance of about 210 pc, whereas the *Hipparcos* parallax $\pi = 0.98 \pm 0.39$ mas (van Leeuwen 2007) puts the star much further, leading to a contradiction.

The spectral type B9 Ve seems to have been used in many subsequent works without revision. Following the hint given by the bad fit of the ultraviolet *IUE* spectrum using models with $T_{\text{eff}} \simeq 10500$ K, typical of a B9AV, it turns out that a temperature around 9000 K gives more sensible results. García-López et al. (2006) reported a fairly high accretion rate log $\dot{M}_{\text{acc}}\,(M_\odot\,\text{yr}^{-1}) = -5.76$, so one has to be careful interpreting the UV spectrum.

A UVES/VLT spectrum (M. van den Ancker 2013, private communication) was used to estimate the stellar gravity, using the width of the Balmer lines, and the metallicity. The conclusion is that a model with $T_{\text{eff}} = 9000$ K, log $g_* = 3.0$, and [Fe/H] = -0.5, fits the spectrum reasonably well—and also the SED—of the star. This set of parameters would correspond to a spectral type around A2 III. Typical errors would be ± 250 K in T_{eff}, ± 0.1 dex in log g_*, and ± 0.3 dex in [Fe/H]. Concerning the metallicity, which is a delicate issue, Folsom et al. (2012) point out the fact that HD 98922 shows suspiciously weak metal lines for their literature temperature, hinting at a potential presence of λ Boo peculiarities. Although that analysis is beyond the
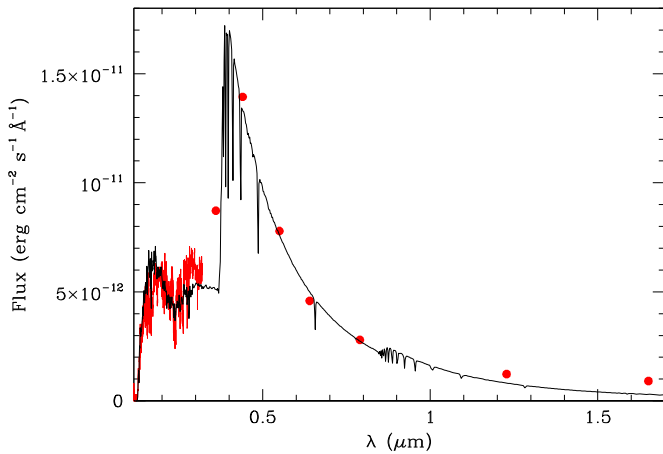
Figure 8. Observed spectral energy distribution of HD 98922 (red line and dots) and the fit of a low-resolution Kurucz model (black) computed with $T_{eff} = 9000$ K, $\log g_* = 3.0$, [Fe/H] $= -0.5$ reddened with $E(B - V) = 0.07$ ($R_V = 3.1$) and normalized to the flux at I. The ultraviolet spectrum is a composite of the *IUE* spectra SWP 18553, SWP50065, SWP50083, LWR14624, LWP30007, and LWP30026 that were retrieved from the archive at the CAB Science Data Centre (http://sdc.cab.inta-csic.es/ines/).
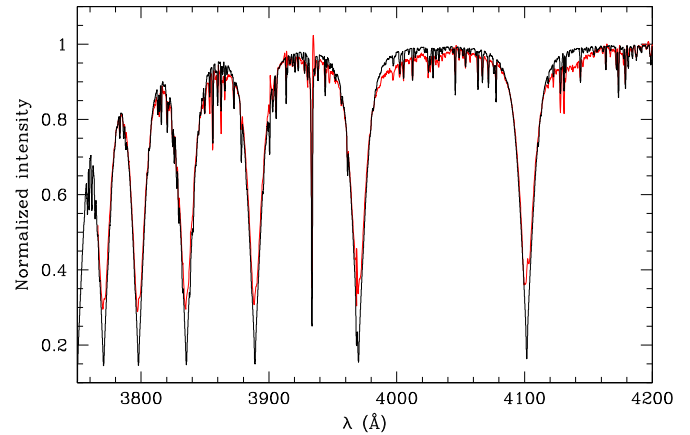

Figure 9. 3750–4200 Å region of the spectrum of HD 98922 obtained with UVES/VLT (red) and the synthetic spectrum (black) computed with the Kurucz ATLAS9 and SYNTHE codes for $T_{eff} = 9000$ K, $\log g_* = 3.0$, [Fe/H] $= -0.5$ (see the text for details).

scope of this work, a fit of the region 6140–6180 Å, which contains three O I (6156.0, 6156.8, and 6158.2 Å) and two Fe II lines, shows that whereas the Fe II features are well reproduced with an abundance [Fe/H] $= -0.5$ or even lower, the oxygen abundance—scaled to the iron abundance—seems to be much larger.

Figures 8 and 9 show the fits to the ultraviolet and optical observations and the spectral fit to the Balmer lines Hδ, Hϵ, and H_8–H_{11}. Low-resolution synthetic spectra from the grid of Castelli–Kurucz and high-resolution synthetic spectra computed using the ATLAS9 and SYNTHE codes by Kurucz (1993) were used.

Using the results from the spectral and SED fits, we can obtain an estimate of the distance. The process is explained in detail in Montesinos et al. (2009) and makes use of the position of the star in the HR diagram $\log g_* - \log T_{eff}$, which can be translated to a point in the HR diagram $\log L_*/L_\odot - \log T_{eff}$ to obtain an estimate of the luminosity. Once $L_*/L_\odot$ is known, the distance can be estimated through the expression $L_* = 4\pi F_{phot} d^2$, where F_{phot} is the stellar flux observed and can be found by integrating the dereddened photospheric model that was fitted to the photometry.

In the left panel of Figure 10, an HR diagram $\log g_*$–$\log T_{eff}$ with the pre-main-sequence evolutionary tracks from the Yonsei–Yale (Yi et al. 2001) collection for $Z = 0.007$—which corresponds roughly to [Fe/H] $= -0.5$—has been plotted. The tracks correspond to 4.0, 4.2, 4.4, 4.6, 4.8, 5.0, and 5.2 $M_\odot$. The point (9000 K, 3.0) is higher than the beginning of the tracks, so to carry out the estimate we have instead used a slightly higher value of $\log g_*$, namely 3.20. The point (9000 K, 3.20 ± 0.1) translates in the HR diagram to $\log L_*/L_\odot - \log T_{eff}$, and in the right panel to a point with $\log L_*/L_\odot = 2.75 \pm 0.20$; therefore, the luminosity of the star would be $L_*/L_\odot = 562^{+329}_{-208}$. The distance implied is $d = 507^{+131}_{-104}$ pc. From this exercise we can also estimate the mass (around 5 $M_\odot$), whereas the age seems to be less than 1 Myr.

We must note that the parameters we give in this paper have been estimated under the hypothesis that this star is a single object. A binary scenario has also been proposed for HD 98922 (e.g., Blondel & Djie 2006), which could potentially explain the

observed SED, the ultraviolet spectrum, and would place the system farther away (beyond 600 pc). This and other possible scenarios for the stellar nature of the HD 98922 system will be deferred to a future publication.

Similar to the modeling presented for HD 104237 (Section 5.1), we have used the MCFOST radiative transfer code (Pinte et al. 2006) to reproduce both the observed SED and the ^{12}CO(3–2) emission the HD 98922 disk (Figure 11). Photometric data available from the literature is listed in Table 4, and, together with the PACS photometry, was incorporated in our SED fitting. Table 5 shows the disk parameters that reproduce the SED and the CO data.

We find that the SED and CO emission can be fit with a dust disk mass of 2×10^{-5} $M_\odot$ of 320 AU in radius. Similar to HD 104237, no flaring with increasing radius is required to fit the SED. No CO freeze out is required to fit the CO spectrum. Since the infrared emission is optically thick, the lack of longer wavelength data makes it very difficult to estimate the dust mass. The ^{12}CO(3–2) data alone cannot be used to constrain the total disk mass. It is found to be optically thick in disks, hence tracing the surface temperature and not the underlying density field near the midplane. Moreover, it depends on many variable parameters such as the assumption of $T_{gas} = T_{dust}$, CO freezout temperatures, the dust-to-gas ratio, and the CO abundance with respect to H_2. Longer wavelength follow up (e.g., submillimeter) is required to further constrain the mass of the disk.

6. DISCUSSION

We surveyed a sample of 52 stars covering a broad range of L_{IR}/L_* values. We detect CO(3–2) emission from 20 systems, and 18 (90%) of these have $L_{IR}/L_* > 0.01$. This implies that in the 31 systems with $L_{IR}/L_* > 0.01$, we obtain a detectability rate of 58%. Figure 12 shows the integrated CO intensity versus fractional infrared excess for our targets. We have not included the sources with possible background/foreground cloud contamination, and also removed HD 155448. The CO intensities have been normalized to a distance of 100 pc.[21] Our results are in agreement with the previous northern survey of

---

[21] The conversion factors used to convert from Kelvin to Jansky were 78.3 for ASTE (from T_A^*), 40.6 for APEX (from T_A^*), and 18.5 for the James Clerk Maxwell telescope (from T_{mb}; since those are the units listed in Dent et al. 2005; conversion factor obtained from http://docs.jach.hawaii.edu/JCMT/HET/GUIDE/het_guide.ps).
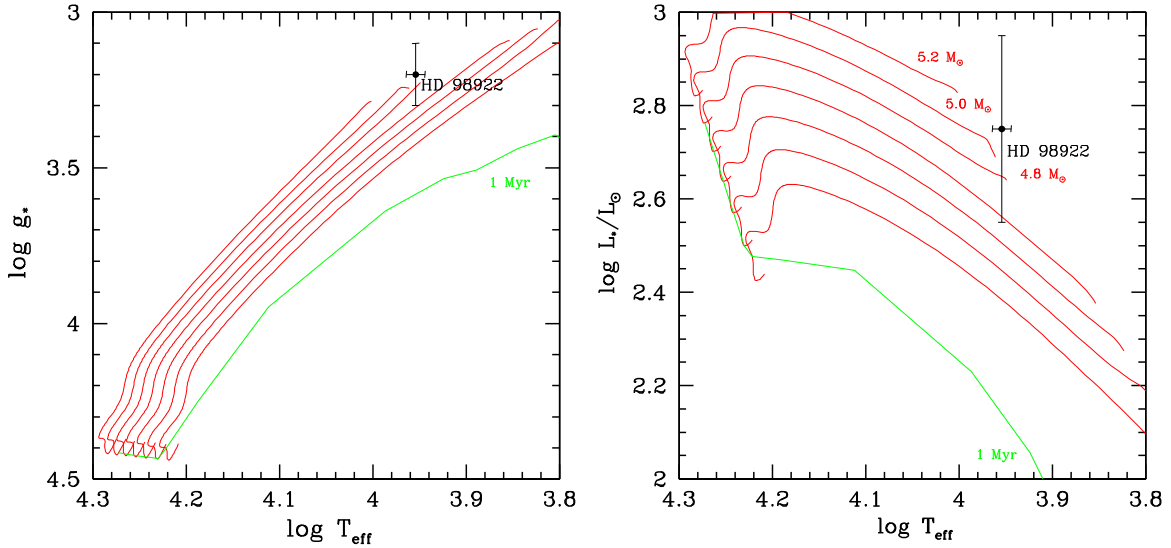
Figure 10. $\log g_* - \log T_{\rm eff}$ and $\log L_*/L_\odot - \log T_{\rm eff}$ HR diagrams showing the evolutionary tracks for 4.0, 4.2, 4.4, 4.6, 4.8, 5.0, and 5.2 $M_\odot$ and the 1 Myr isochrone from the Yonsei–Yale collection for $Z = 0.007$. The position of a star with $T_{\rm eff} = 9000$ K and $\log g_* = 3.2$ in the diagram on the left is translated in a one-to-one correspondence to the HR diagram on the right to obtain the luminosity. The value of L_* and the estimate of the dereddened observed photospheric flux, $F_{\rm phot}$, allow us to calculate the distance to the star (see the text for details). The position of the star with respect to the isochrone indicates that the star is younger than 1 Myr.
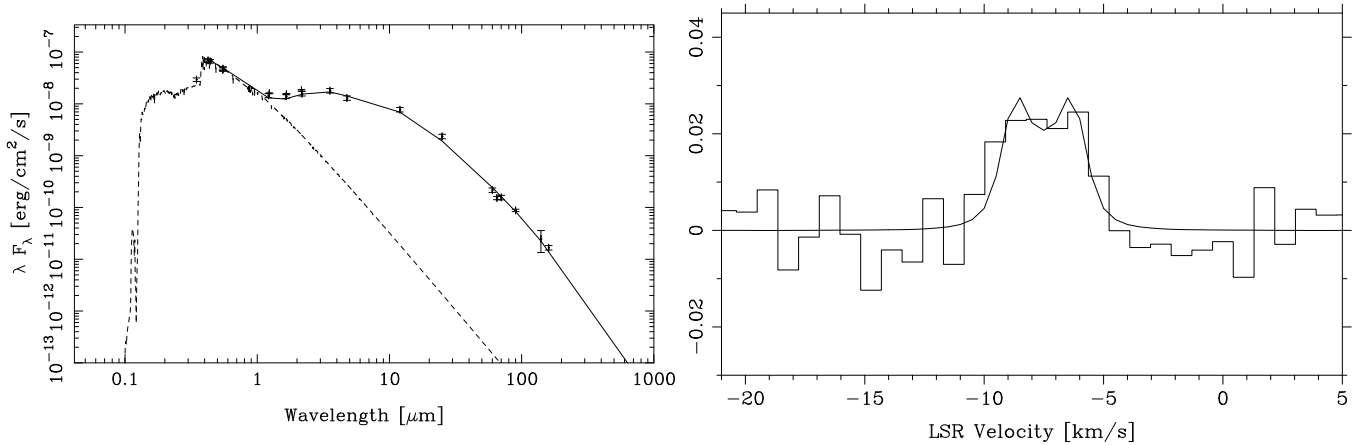
Figure 11. Left: observed SED of HD 98922 (black points with error bars) plotted against the MCFOST disk model that fits the optical to far-IR data (solid line). Right: velocity distribution of the ^{12}CO(3–2) line detected from the disk around HD 98922, with the disk model superimposed (solid line). Intensity units are in antenna temperature (T_A^*). The spectrum shown Figure 6 has been smoothed by re-binning into two channel averages.

Dent et al. (2005), where $\sim$50% of the stars $L_{\rm IR}/L_* > 0.01$ have CO detections.

Ten objects (42%) deviate from that trend by having $L_{\rm IR}/L_* > 0.01$ but no detectable CO emission. HD 100453 and HD 95881 have indeed been identified as disks in transition from gas-rich to gas-poor (Collins et al. 2009; Verhoeff et al. 2010). HD 95881 appears to be in a particular transition from a gas-rich flaring disk to a gas-poor self-shadowed disk (Verhoeff et al. 2010), which would explain the relatively large infrared excess and the lack of detectable CO. Overall, the results from this and previous surveys indicate that the infrared excess is an indicator for detecting CO gas, in agreement with previous studies that suggest that young stars with large amounts of circumstellar dust emission also hold large reservoirs of circumstellar molecular gas (Dent et al. 2005).

Only four of the newly detected systems are, however, clearly free of CO emission from extended gas associated with ambient molecular cloud material. The contaminated sources may indeed harbor significant quantities of CO, but higher resolution interferometric observation would be needed

to filter out any cloud contamination from the disk emission. Alternatively, higher density tracers such as HCO$^+$ or CN could be considered, as in Guilloteau et al. (2013) and de Gregorio-Monsalvo et al. (2013). High density tracers will detect the emission from the disk, while the possible contaminating clouds are not dense enough to be detected in these molecules. This is one of the main results from the pilot program from Guilloteau et al. (2013). In addition, higher order transition in CO and HCO+ can also be used to avoid contamination from cold clouds, as the temperatures required to excite these transitions are larger than usually found in molecular clouds (see Appendix A.2).

Most of the sources showing cloud contamination are all well studied disks known to harbor gas emission (e.g., HD 250550, HD 97048, HD 142527, HD 144668, HD 149914, KK Oph, and VV Ser). Our single-dish observations indicate they are still associated with their parent clouds, given the coincidence in position and velocity between the observed spectra and existing molecular cloud maps.

We detect ^{12}CO around HD 104237 and HD 98922 for the first time, and combine it with SED data to produce disk models.
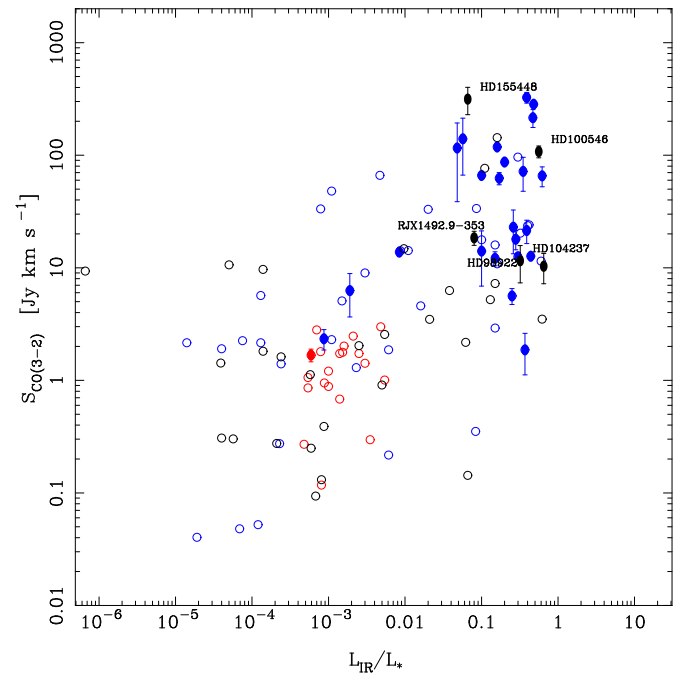
13

Table 4
HD 98922 Photometric Data

Wavelength (μm)	Flux (erg/cm^{-2}/s/Å)	Flux Error (erg/cm^{-2}/s/Å)	Reference Filter	Reference
0.347	6.7298E−12	6.7298E−13	U	Malfait et al. (1998)
0.425	1.3305E−11	1.3305E−12	B	Malfait et al. (1998)
0.440	1.2489E−11	1.2489E−12	B	Høg et al. (2000)
0.550	7.3858E−12	7.3858E−13	V	Malfait et al. (1998)
0.550	7.5370E−12	7.5370E−13	V	Høg et al. (2000)
0.548	7.1682E−12	3.3011E−13	y	Hauck & Mermilliod (1998)
1.215	1.1478E−12	1.1478E−13	J	Malfait et al. (1998)
1.235	1.2427E−12	2.2893E−14	J	Cutri et al. (2003)
1.654	8.2592E−13	8.2592E−14	H	Malfait et al. (1998)
1.662	9.0252E−13	2.4109E−14	H	Cutri et al. (2003)
2.159	8.3236E−13	2.7604E−14	K_s	Cutri et al. (2003)
2.179	7.1211E−13	7.1211E−14	K	Malfait et al. (1998)
3.547	4.9889E−13	4.9889E−14	K	Malfait et al. (1998)
4.769	2.6797E−13	2.6797E−14	M	Malfait et al. (1998)
12.000	6.3403E−14	6.3403E−15	12 μm	Beichman et al. (1988)
25.000	9.2532E−15	9.2532E−16	25 μm	Beichman et al. (1988)
60.000	3.5550E−16	3.5550E−17	60 μm	Beichman et al. (1988)
65.000	2.3016e−16	1.6985e−17	65 μm	Yamamura et al. (2011)
70.000	2.1909e−16	1.0954e−17	70 μm	PACS (This work)
90.000	9.5968e−17	5.2938e−18	90 μm	Yamamura et al. (2011)
140.000	1.7314e−17	7.9813e−18	140 μm	Yamamura et al. (2011)
160.000	1.0270e−17	5.1351e−19	160 μm	PACS (This work)

Table 5
HD 98922 Disk Model

Physical Parameter	Value	Reference
Stellar Properties		
Spectral type	A2 III	This work
Primary star mass: M ($M_\odot$)	5.0	This work
Effective temperature: T (K)	9000	This work
Stellar radius: R ($R_\odot$)	9.0	This work
Distance: d (pc)	$d = 507$	This work
Disk Structure		
Disk total mass: M_D ($M_\odot$)	$100 \times M_d$	This work
Disk dust mass M_d ($M_\odot$)	2×10^{-5}	This work
Inner rim: $R_{\rm in}$ (AU)	1.5	This work
Characteristic radius R_C (AU)	320	This work
Characteristic height h_C (AU)	0.15	This work
Surface density exponent: γ	1.0	This work
Flaring exponent: ψ	0.0	This work
Inclination angle: i (deg)	20	This work
Systemic velocity: $V_{\rm lsr}$	−8	This work

Figure 12. Integrated CO intensity, or upper limits vs. fractional infrared excess, for the observed stars (only stars with no cloud contamination and with both distance estimates and enough SED points for reliable determinations have been included). Black filled circles denote objects with positive detections likely to be associated with circumstellar CO disks, while black open circles are 1σ upper limits (computed using 10 km s^{-1} windows; see the text). Data from the literature for protoplanetary and debris disk from the CO surveys of Dent et al. (2005) and Moór et al. (2011) are plotted in blue and red, respectively.

We confirm that geometrically flat disk models can indeed reproduce both the SEDs and CO profiles. The incorporation of CO freeze out is required to account for observed CO intensities of HD 104237, and is expected to play a significant role if, according to new models, the CO is located closer to the midplane where the temperatures are lower. The 63.2 μm [O I] and the [O I] 6300 Å line are also detected in both disks. Meeus et al. (2012) found a strong correlation between 63.2 μm [O I] and ^{12}CO(3–2) in a sample of 20 Herbig Ae/Be stars, but no clear correlation between ^{12}CO and [O I] 6300 Å. Even though the origin of the [O I] 6300 Å line is unclear, it is usually thought to originate in the surface of the disks (Acke et al. 2005) and to trace the inner regions of the disk (1–50 AU; van der Plas et al. 2008). The fact that we are indeed detecting both [O I] lines and the ^{12}CO(3–2) may indicate that the ^{12}CO(3–2) emission stems from the warmer layers of the disk, although these lines

come from different radius ranges with CO(3–2) being formed the farthest outside ($R \geqslant 100$ AU; e.g., Hughes et al. 2008b).

HD 104237 is part of a multiple system, and our LABOCA imaging shows that at least two sources in the field of view have detectable submillimeter emission. Our SED modeling

indicates a total disk mass of $4 \times 10^{-2}\, M_\odot$ around the primary component. We can also use the 870 μm flux to estimate the mass of the disk around component E (which may also include a contribution from component D). Assuming $T \sim 20$ K, an opacity of 0.35 m^2 Kg^{-1}, and a 100:1 gas-to-dust ratio (e.g., Andrews & Williams 2005), implies a 0.004 $M_\odot$ disk mass for component E(+D).

The HD 104237 system bears a striking resemblance to RW Aur. RW Aur A is a very active classical T Tauri driving a powerful optical jet. It is separated by 1″2 from RW Aur B, and there is also some suspicion that RW Aur A may have a close companion (from radial velocity variations). Radio interferometric observations of the ^{12}CO and ^{13}CO lines in RW Aur with the Plateau de Bure interferometer (PdBI; Cabrit et al. 2006) show that the RW Aur A disk is very compact ($R_{\rm out} \sim 40$–57 AU), probably due to truncation by RW Aur-B. Despite the truncation, a large-scale spiral arm extending over 500 AU was detected in ^{12}CO connecting the RW Aur A and RW Aur B disks, interpreted as tidal disruption of the RW Aur-A disk by the companion, to be searched for in the HD 104237 multiple system.

Based on the 1″26 separation between HD 104237A and HD 104237B, Grady et al. (2004) predicted a tidal truncation outer radius of 38 AU for HD 104237A. This is significantly smaller than the 90 AU characteristic radius we derive from the SED modeling. However, the truncation radius prediction is subject to uncertainties on the projected distance, while the outer radius disk estimates are known to be poorly constrained by pure SED fitting. Resolved imaging is required to directly measure the outer truncation radius of the disk.

7. CONCLUSIONS

We conducted a single-dish survey for ^{12}CO(3–2) gas in a sample of 52 protoplanetary and debris disks. We report a 58% detection rate in sources with an infrared excess fraction larger than 0.01. Most of those detections can, however, be associated with a parent molecular cloud, and therefore can only be considered upper limits to the disk emission. We identify four CO detections that can be explained as arising from circumstellar CO gas. We present the detection of two new gas-rich disks, HD 104237 and HD 98922, and use radiative transfer codes to model their continuum and gas emission. Both disks are unusual, geometrically flat, CO-rich disks with 63.2 μm [O I] and [O I] 6300 Å line emission. HD 104237 and HD 98922 are unique laboratories for studying extreme SED-predicted flat disks. Are the SEDs of "flat" disks different from those of "flared" disks because of dust settling into the midplane or are they just smaller in radii? Resolved submillimeter images with existing interferometers (e.g., ALMA) are required to further constrain the physicochemical structure of these disks and ultimately understand the gas-clearing processes that yield planet formation.

APPENDIX

A.1. Detections with Background/Foreground Contamination

In this appendix, we present individual sources with CO detections likely to arise from background/foreground contamination.

A.1.1. HD 124237

HD 124237 is located on the Galactic plane (Dame et al. 2001), yielding several velocity components of galactic CO detected in our spectra (Figure 13). The line intensities are typical of galactic clouds, and, if present, any circumstellar CO emission would be completely dominated by the ambient emission. The intensities of the lines vary significantly when using a different reference position, indicating of strong contamination from ambient CO.

A.1.2. HD 178253

This A2V star, alias α CrA, was originally cataloged as a debris disk type star by Mannings & Barlow (1998) based on data from *IRAS*, and subsequently re-observed with *Spitzer* by Rieke et al. (2005). Mid-infrared imaging using Gemini South failed to detect any significant mid-IR excess toward this star (Moerchen et al. 2010).

HD 178253 is located in the direction of the CrA molecular cloud (Harju et al. 1993), which is clearly seen in the spectrum of the reference (off) position. HD 178253 has a photospheric radial velocity of $V_{\rm helio} = -18.4 \pm 2$ km s^{-1} (Barbier-Brossat & Figon 2000), or $V_{\rm lsr} = -12.3$ km s^{-1}. No prominent emission is detected near the tabulated stellar velocity. In addition, as seen in Figure 13, the resulting spectrum changes dramatically when using a different reference position. Therefore, the CO detection cannot be unambiguously associated with a circumstellar disk.

A.1.3. HD 36917, HD 37411, HD 37389, HD 37258, and HD 38087

HD 36917, HD 37411, HD 37389, HD 37258, and HD 38087 are located in the Orion molecular clouds. The spectra toward these stars are contaminated due to cloud emission in the reference. This is obvious in the case of HD 36917 (Figure 13), where a second observation with a different reference position was acquired. Changing the off position yielded false absorption features indicative of strong emission in the reference. A similar effect is seen when comparing the two spectra taken toward HD 37411 (Figure 14).

Located in the middle of Orion's waist, between Alnilam and ζ Ori, HD 37389 is surrounded by the strong background
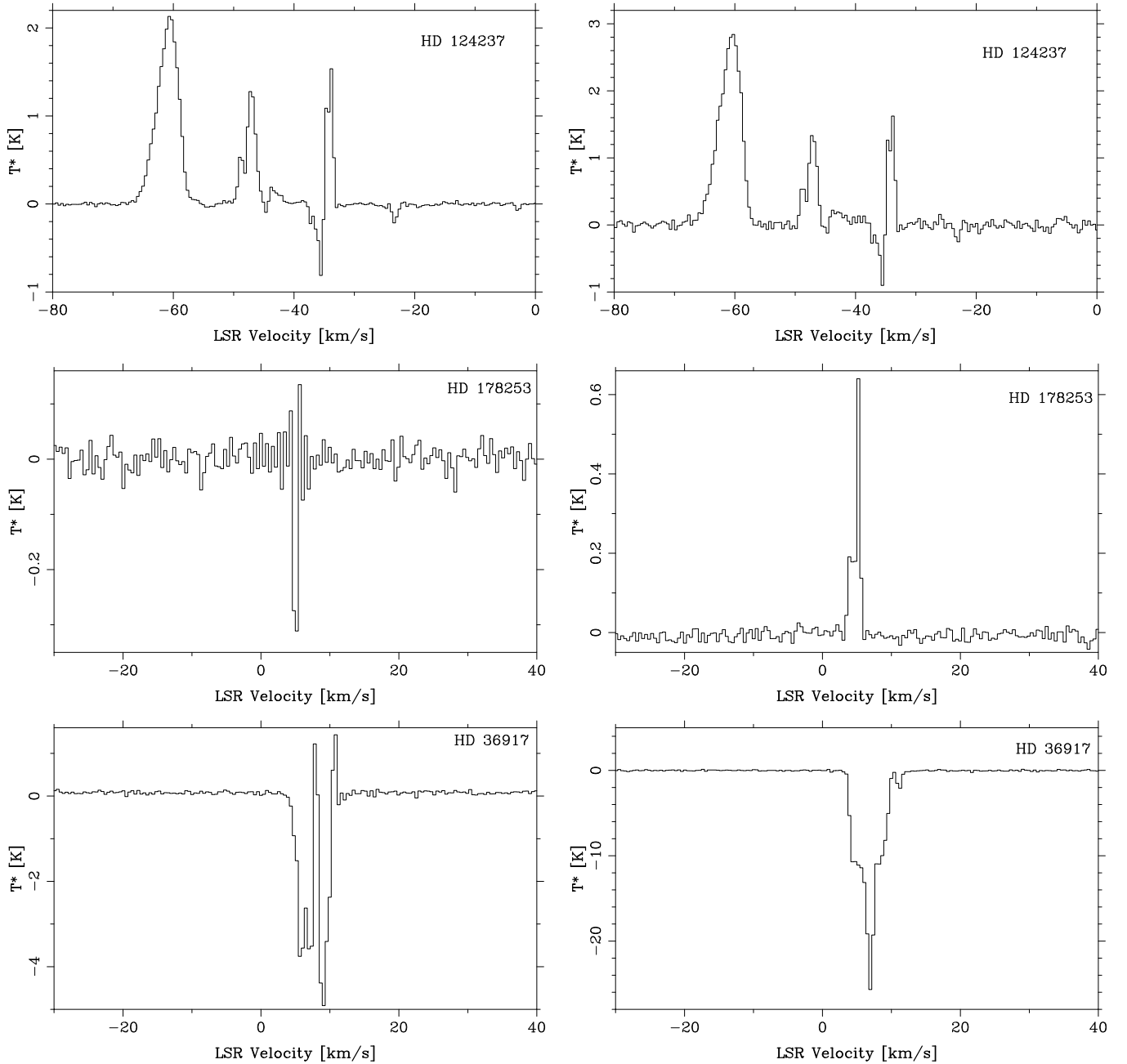
Figure 13. Detections with background/foreground contamination in the reference position. The left panels show the spectra obtained using a −180 arcsec reference position, while the panels on the right present the spectra resulting from a +180 arcsec reference position. When available, the stellar velocity has been plotted with a vertical line (in V_{lsr}). Intensity units are in antenna temperature (T_A^*).

from Orion B. The single-pointing APEX CO(3–2) spectrum gives a narrow line, with a velocity-integrated T_{mb} intensity of 4.2 K km s^{-1} (Figure 15). CO(3–2) probably stems from the diffuse cloud.

Our CHAMP+ follow-up observations (Casassus et al. 2013) show how the diffuse emission is clearly traced in the north-western horns of the CHAMP+ footprint (see Appendix A.2 for details).

For HD 37258 and HD 38087 the detected peaks appear too large compared to pure disk emission (Figures 15 and 16). Bogus absorption features due to reference contamination are seen in both spectra. The smaller peaks at 7 km s^{-1} are too narrow to be circumstellar, and also coincide with the 4–14 km s^{-1} range of the known clouds in Orion (Dame et al. 2001). CO

emission toward these stars is most likely associated with the Orion Molecular Cloud.

A.1.4. HD 85567

HD 85567 is a B2Ve star first associated with the HAeBe membership by Thé et al. (1994). Its infrared excess of 3.3 × 10^{-1} is characteristic of young, massive protoplanetary disks. Juhász et al. (2010) report strong silicate emission detected with the *Spitzer Space Telescope*.

We detect a bright single peaked line at 31 km s^{-1} (Figure 16). HD 85567 is located close to the Galactic plane in the direction of the Carina arm at $(l, b) = (282.6, -5.4)$. CO mappings of the Carina region have not covered the position of HD 85567 (Fukui
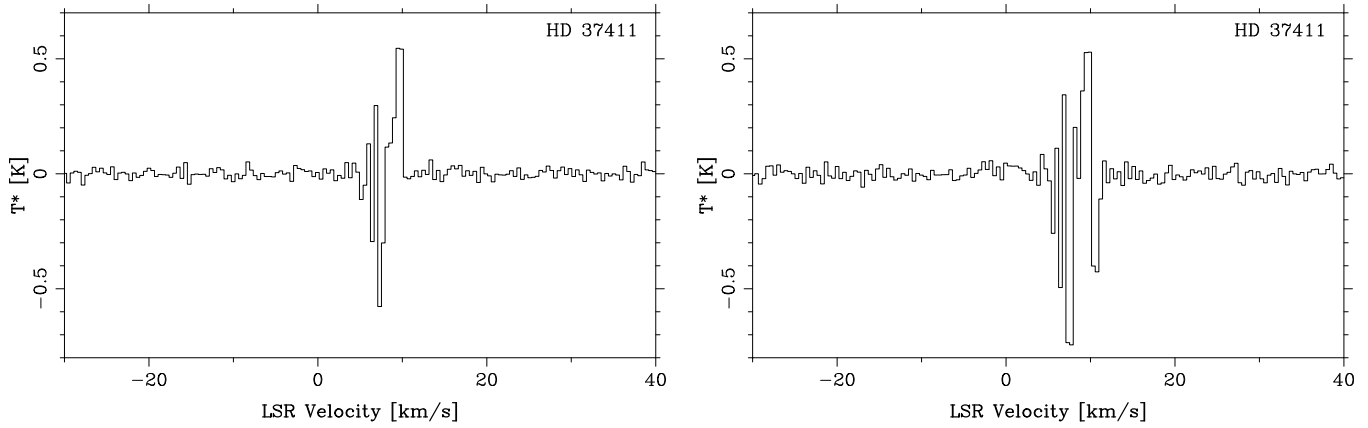
16

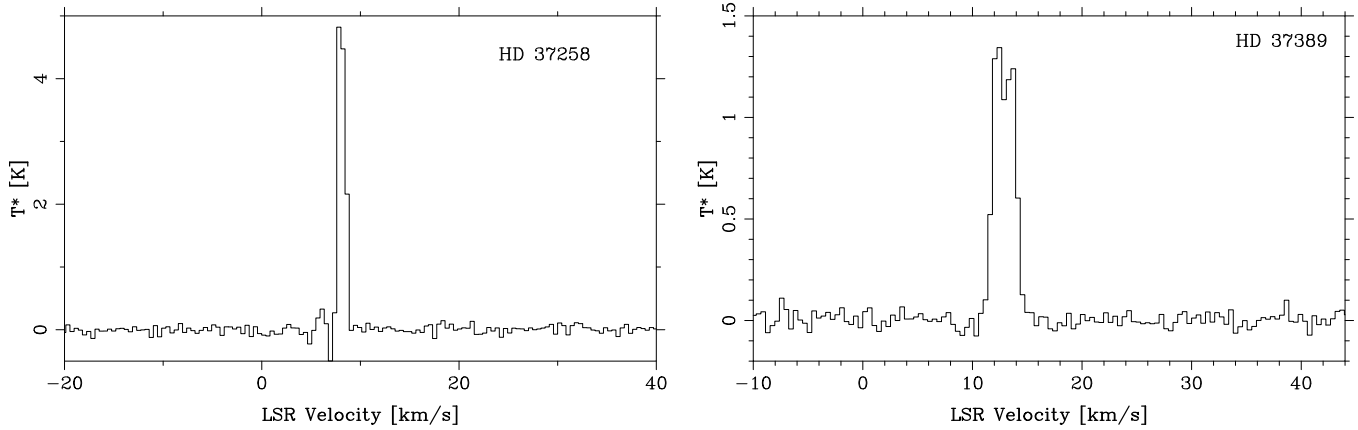**Figure 14.** Same as Figure 13.
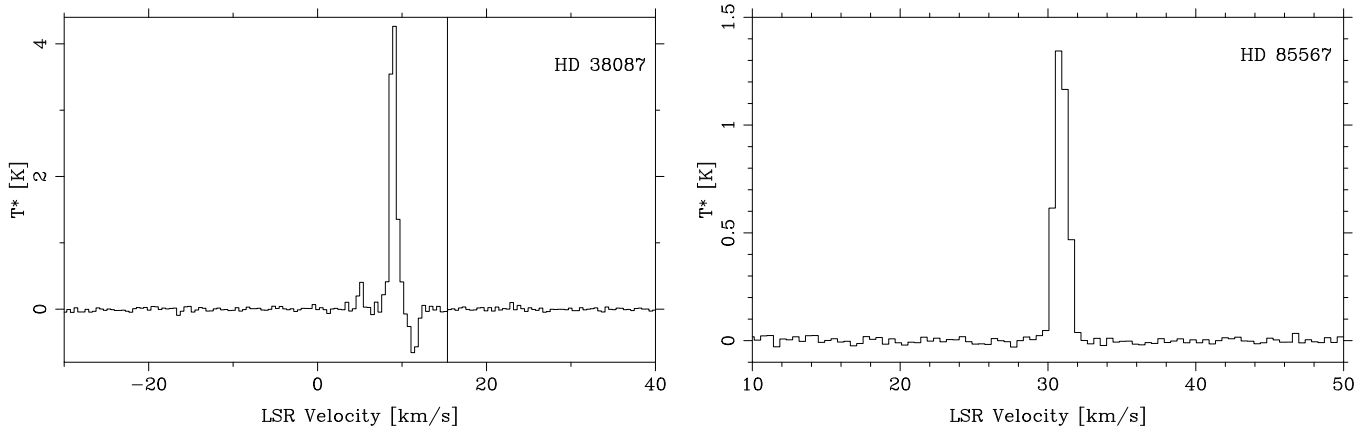

Figure 15. Same as Figure 13.

Figure 16. Same as Figure 13. The stellar velocity for HD 38087 was obtained from Gontcharov (2007).

et al. 1999; Zhang et al. 2001; Dawson et al. 2008), therefore no comparison with known cloud velocities is available.
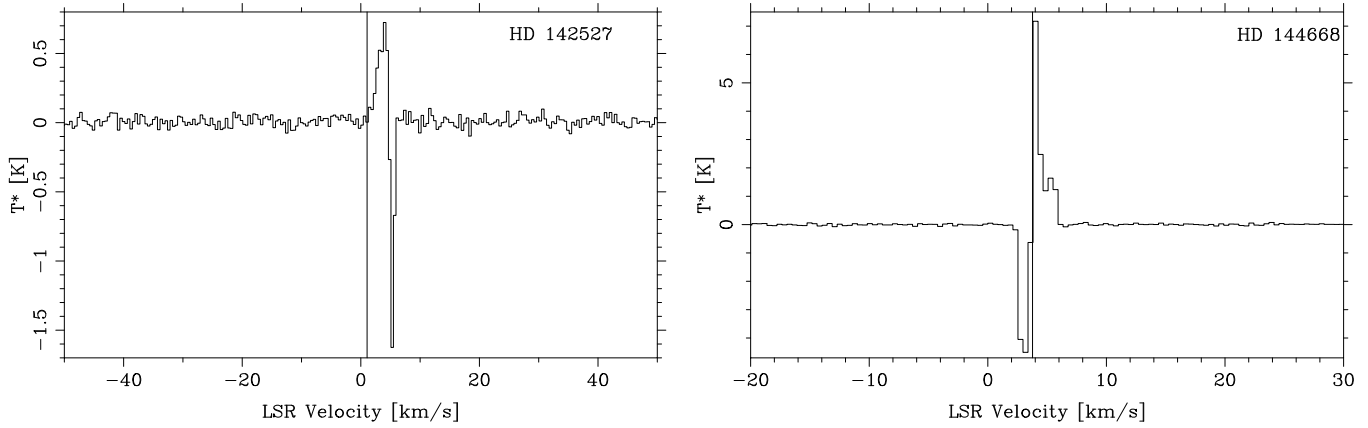
A.1.5. HD 142527

HD 142527 is surrounded by a well-studied circumstellar disk that harbors copious amounts of gas, as detected with the SMA (Ohashi 2008; Öberg et al. 2011). The ASTE spectrum shows clear contamination in the reference position (Figure 17). The emission coincides with the radial velocity of the star.

Our observations toward HD 142527 highlight the difficulties in using CO(3–2) single-dish observational techniques to detect unambiguously circumstellar disk emission in environments with high ambient emission. However, our follow-up CO(6–5) observations using CHAMP+ in APEX confirm warm CO emission in the position of the star (Casassus et al. 2013), as well as the detection of a double-peaked HCO+(4–3) line (de Gregorio-Monsalvo et al. 2013). This may suggest that warmer gas or higher density gas tracers may indeed be combined with single-dish observations to detect circumstellar gas emission from protoplanetary disks.

Recent ALMA imaging of this gas-rich disk has revealed the existence of CO gas inside the dust cavity, as well as the presence of gap-crossing HCO+ filaments (Casassus et al. 2013).

Figure 17. Same as Figure 13. The stellar velocity for HD 142527 was obtained from Gontcharov (2007).
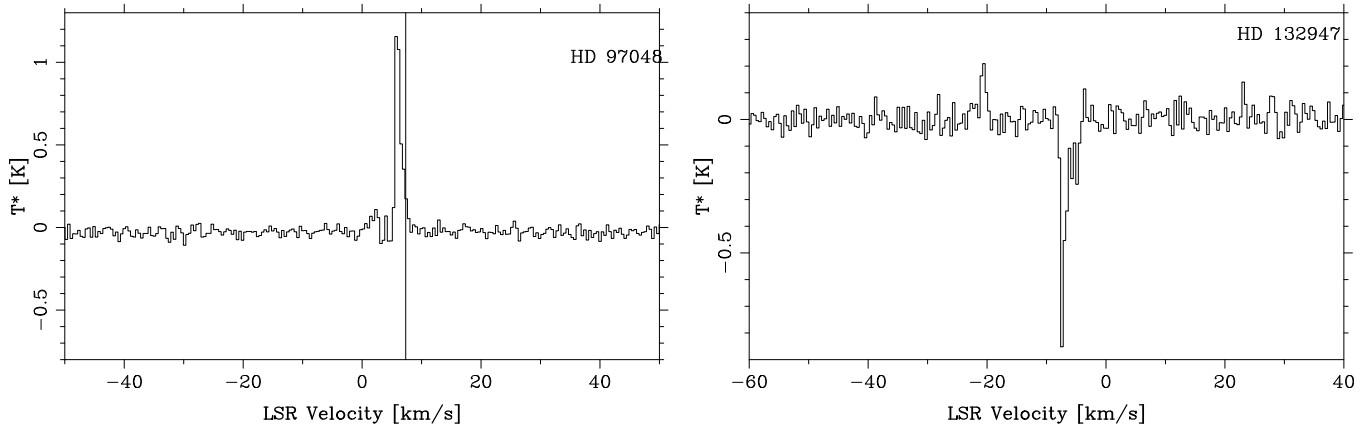
Figure 18. Same as Figure 13. The stellar velocity for HD 97048 was obtained from Carmona et al. (2011).

A.1.6. HD 144668

HD 144668 (V856 Sco, HR5999) is an A7 IVe star that exhibits a large infrared excess ($L_{IR}/L_* \sim 0.51$), with an age of 2.8 Myr. Strong [O I] 63.2 μm emission toward HD 144668 is detected (Meeus et al. 2012), indicative of its disk still having a large reservoir of orbiting gas.

HD 144668 is located in the direction of the Lupus molecular clouds (Figure 2; Hara et al. 1999). The emission in the CO(3–2) detection spectrum does coincide within errors with the tabulated stellar velocity (Figure 17). However, it also coincides both in position and velocity with the C^{18}O core 27 in Hara et al. (1999) ((l, b) = (339.567,933), V_{lsr} = 4.12 km s^{-1}). This suggests that the CO emission observed toward the star is dominated by diffuse cloud emission. The detection can be considered as an upper limit to the disk intrinsic CO emission.

A.1.7. HD 97048

HD 97048 (CU Cha) is a well-studied A0 star located in the direction of the Chameleon I cloud (Figure 2; Mizuno et al. 1998). Martin-Zaïdi et al. (2009) detected the mid-IR H$_2$ S(1) line at 17 μm, but not the S(2) nor the S(4) at 12 and 8 μm, respectively. Carmona et al. (2011) detect near-IR H$_2$ 1–0 S(1) using CRIRES on the VLT. Copious amounts of CO J = 19–17, [O I] 145.5 μm, and [O I] 63.2 μm emission toward HD 97048 are detected (Meeus et al. 2012). It is also one of the three objects where [C II] 157.7 μm is detected.

The CO spectra is contaminated due to cloud emission in the reference (Figure 18), since the star lies on top of the Cha I molecular cloud. The typical ^{12}CO(1–0) cloud velocities in the Cha I region are in the V_{lsr} = 2–6 km s^{-1} range (Mizuno et al. 1998), which agrees with the (contaminated) emission we detect.

A.1.8. HD 132947

HD 132947 is located in the fourth galactic quadrant toward the Circinus molecular cloud (Figure 2; Shimoikura & Dobashi 2011). The NANTEN ^{12}CO maps show several velocity components ranging between V_{lsr} = −4 and −6.5 km s^{-1}, in agreement with the contamination seen in the reference position (which produces the false absorption feature seen in the spectrum). A small emission feature is seen near V_{lsr} = −22 km s^{-1}, but the lack of information on the stellar velocity hampers any association with possible circumstellar emission (Figure 18).

A.1.9. HD 250550

HD 250550 is located toward the Gemini OB1 molecular clouds (Carpenter et al. 1995). Based on existing ^{12}CO(1–0) maps, the velocity of the CO(3–2) emission detected in our spectra (Figure 19) coincides with the known cloud velocity in the direction of HD 250550 (V_{lsr} = 4.12 km s^{-1}; Carpenter et al. 1995).
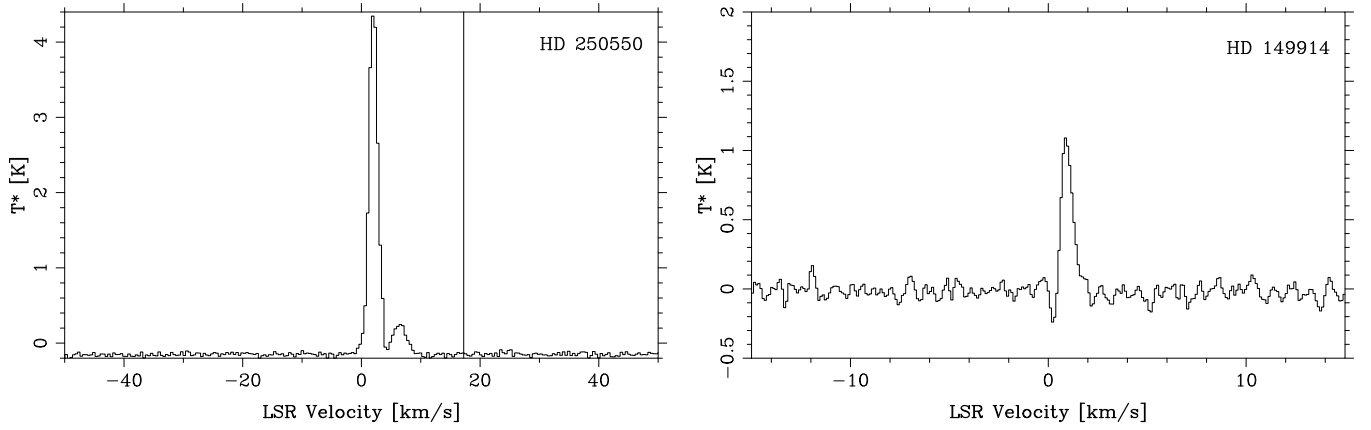
Figure 19. Same as Figure 13. The stellar velocity for HD 250550 was obtained from Gontcharov (2007).
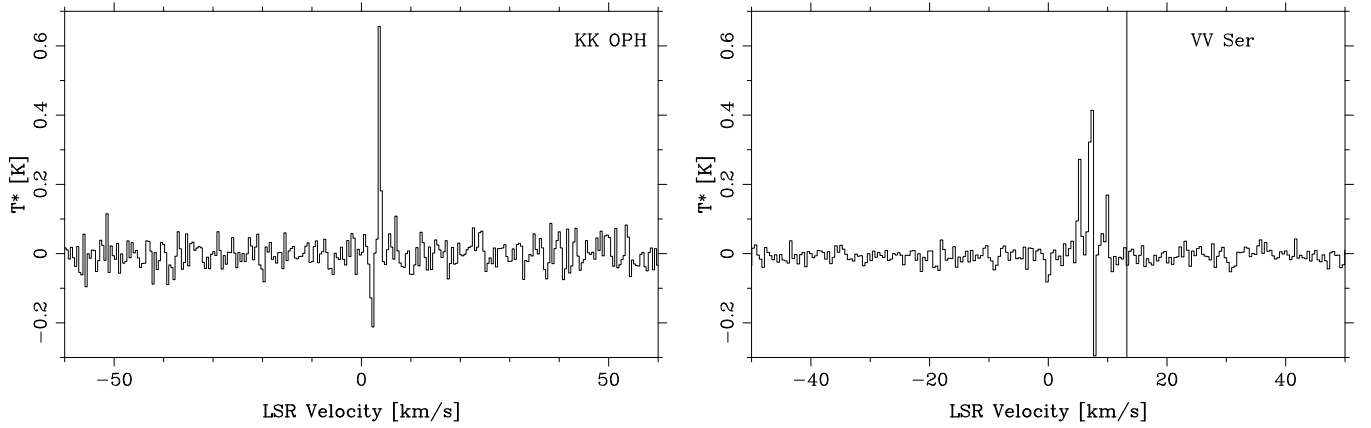
Figure 20. Same as Figure 13. The stellar velocity for VV Ser was obtained from Acke et al. (2005).
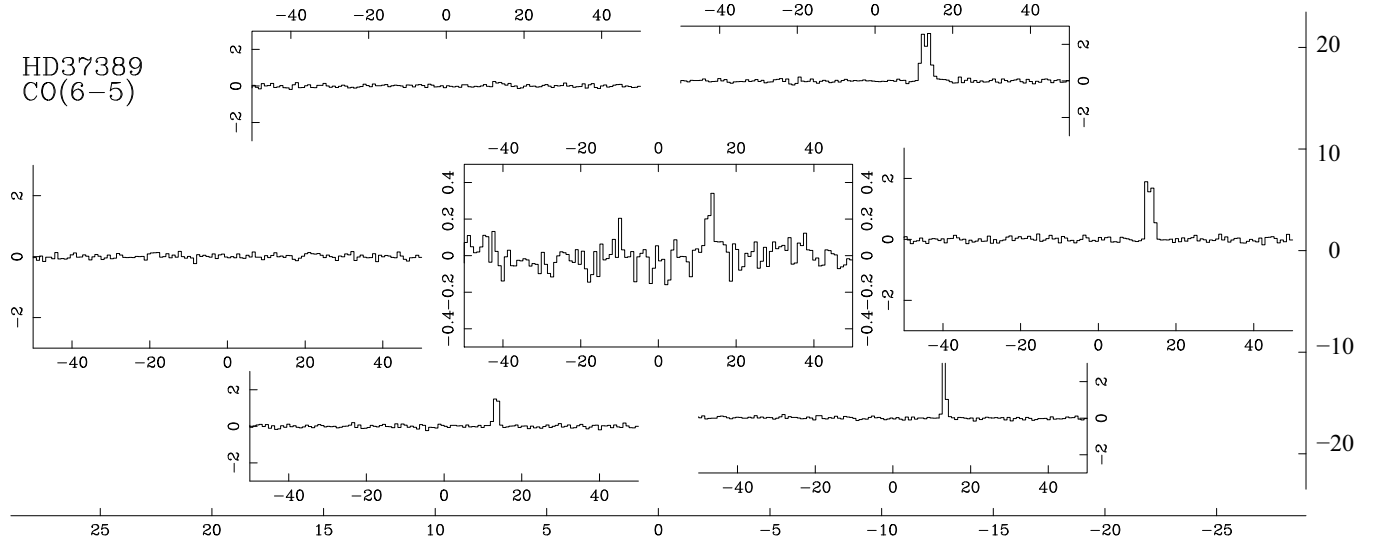
Figure 21. CHAMP+ seven-horn footprint for HD 37389 in CO(6–5). The outermost axes show offset R.A. and decl., in arcsec. The other axes give $T_A^\star$ on the y-axis and V_{lsr} on the x-axis. The emission from the Orion Molecular Cloud is clearly traced by the CHAMP+ footprint.

A.1.10. HD 149914

^{12}CO(3–2) emission is detected toward the B9.5 IV star HD 149914, located toward the Ophiucus cloud (Dame et al. 2001). The spectrum shows indications of contamination in the reference position near 0 km s^{-1} (Figure 19). At least four clouds nearby (1–3 degrees) with $V_{lsr} = 1$–5 km s^{-1} are known (Tachihara et al. 2000). The closest core to the line of sight of

HD 149914 is located at $(l, b) = (359.23, 18.63)$ and has a main velocity component $V_{lsr} = 0.58$ km s^{-1} and width 0.92 km s^{-1}.

A.1.11. KK Oph

KK Oph is a binary system located at the edge of the Pipe Nebula at $(l, b) = (357.06, 7.1)$, close to a C^{18}O core with $V_{lsr} \sim 3.6$ km s^{-1} (Onishi et al. 1999). Cloud contamination

is evident in our CO spectra (Figure 20), although the [O I] 63.2 μm detection indicates that the KK Oph system harbors a gas-rich protoplanetary disk (Meeus et al. 2012).

A.1.12. VV Ser

Our observations show that VV Ser is surrounded by extended CO(3–2) that contaminates the reference position (Figure 20), with centroid velocity $V_{lsr} \sim 7$ km s^{-1}. Alonso-Albi et al. (2008) reported continuum detection (PdBI), corresponding to a 4×10^{-5} $M_\odot$ disk, and a CO(1–0) non-detection (at a 1σ noise limit of 0.3 K in 1 km s^{-1} channels). Liu et al. (2011) detect CO(2–1) and CO(3–2) using the KOSMA 3 m telescope and suggest that they might come from three different velocity components at 5.3, 7.3, and 9.5 km s^{-1}, respectively. We detect three ^{12}CO(3–2) peaks at these same velocities. VV Ser is located in the direction of the Aquila Rift, which together with the contaminated spectra indicates that the single-dish observations are dominated by diffuse molecular cloud emission (Dame et al. 2001).

A.2. CHAMP+ Follow-up Observations

Five sources with ^{12}CO(3–2) detections (HD 142527, HD 178253, HD 37389, RX J1842.9−3532, and VV Ser) were observed with the CHAMP+ dual color heterodyne array at 450 μm and 350 μm with $\sim 8''$ resolution. The seven-horn CHAMP+ receiver allows us to map the position of the star and its periphery simultaneously (Güsten et al. 2008), providing a seven-pixel map of the gas emission around each star. The CO(6–5) 691.4 GHz and C I(2–1) 809 GHz were targeted in order to confirm the ^{12}CO(3–2) using the ^{12}CO(6–5) line, and the C I(2–1) to obtain measures of the atomic gas content of the disks. These observations are described in Casassus et al. (2013). Only HD 142527 revealed a compact ^{12}CO(6–5) disk detection, and only C I(2–1) upper limits. HD 37389 shows clear contamination from extended emission, particularly in the northeastern horns of the CHAMP+ footprint (Figure 21).

REFERENCES

Acke, B., & van den Ancker, M. E. 2004, A&A, 426, 151
Acke, B., van den Ancker, M. E., & Dullemond, C. P. 2005, A&A, 436, 209
Alexander, R. 2013, in IAU Symp. 299, Exploring the Formation and Evolution of Planetary Systems, ed. M. Booth, B. C. Matthews, & J. R. Graham (Cambridge: Cambridge Univ. Press), 179
Alonso-Albi, T., Fuente, A., Bachiller, R., et al. 2008, ApJ, 680, 1289
Andrews, S. M., & Williams, J. P. 2005, ApJ, 631, 1134
Andrews, S. M., Wilner, D. J., Hughes, A. M., Qi, C., & Dullemond, C. P. 2009, ApJ, 700, 1502
Armitage, P. J. 2011, ARA&A, 49, 195
Balog, Z., Müller, T., Nielbock, M., et al. 2013, ExA, 38
Barbier-Brossat, M., & Figon, P. 2000, A&AS, 142, 217
Beichman, C. A., Neugebauer, G., Habing, H. J., Clegg, P. E., & Chester, T. J. 1988, Infrared Astronomical Satellite (IRAS) Catalogs and Atlases, Volume 1: Explanatory Supplement (NASA RP-1190; Washington, DC: GPO)
Birnstiel, T., Dullemond, C. P., & Brauer, F. 2010, A&A, 513, A79
Blondel, P. F. C., & Djie, H. R. E. T. A. 2006, A&A, 456, 1045
Böhm, T., Catala, C., Balona, L., & Carter, B. 2004, A&A, 427, 907
Boss, A. P. 2001, ApJ, 563, 367
Boss, A. P. 2005, ApJ, 629, 535
Boggess, A., Carr, F. A., Evans, D. C., et al. 1978, Natur, 275, 372
Brittain, S. D., Simon, T., Najita, J. R., & Rettig, T. W. 2007, ApJ, 659, 685
Cabrit, S., Pety, J., Pesenti, N., & Dougados, C. 2006, A&A, 452, 897
Carmona, A. 2010, EM&P, 106, 71
Carmona, A., van den Ancker, M. E., Henning, T., et al. 2008, A&A, 477, 839
Carmona, A., van der Plas, G., van den Ancker, M. E., et al. 2011, A&A, 533, A39
Carpenter, J. M., Snell, R. L., & Schloerb, F. P. 1995, ApJ, 445, 246
Casassus, S., Hales, A., de Gregorio, I., et al. 2013, A&A, 553, A64

Casassus, S., van der Plas, G., M, S. P., et al. 2013, Natur, 493, 191
Collins, K. A., Grady, C. A., Hamaguchi, K., et al. 2009, ApJ, 697, 557
Coulson, I. M., Walther, D. M., & Dent, W. R. F. 1998, MNRAS, 296, 934
Cutri, R. M., Skrutskie, M. F., van Dyk, S., et al. 2003, The IRSA 2MASS All-Sky Point Source Catalog, NASA/IPAC Infrared Science Archive, http://irsa.ipac.caltech.edu/applications/Gator
D'Alessio, P., Calvet, N., Hartmann, L., Franco-Hernández, R., & Servín, H. 2006, ApJ, 638, 314
D'Alessio, P., Calvet, N., Hartmann, L., Lizano, S., & Cantó, J. 1999, ApJ, 527, 893
Dahm, S. E., & Carpenter, J. M. 2009, AJ, 137, 4024
Dame, T. M., Hartmann, D., & Thaddeus, P. 2001, ApJ, 547, 792
Dawson, J. R., Kawamura, A., Mizuno, N., Onishi, T., & Fukui, Y. 2008, PASJ, 60, 1297
de Gregorio-Monsalvo, I., Ménard, F., Dent, W., et al. 2013, A&A, 557, A133
de Winter, D., van den Ancker, M. E., Maira, A., et al. 2001, A&A, 380, 609
de Zeeuw, P. T., Hoogerwerf, R., de Bruijne, J. H. J., Brown, A. G. A., & Blaauw, A. 1999, AJ, 117, 354
Dent, W. R. F., Greaves, J. S., & Coulson, I. M. 2005, MNRAS, 359, 663
Dobashi, K., Uehara, H., Kandori, R., et al. 2005, PASJ, 57, 1
Draine, B. T., & Lee, H. M. 1984, ApJ, 285, 89
Dunkin, S. K., Barlow, M. J., & Ryan, S. G. 1997, MNRAS, 290, 165
Dutrey, A., Guilloteau, S., Duvert, G., et al. 1996, A&A, 309, 493
Fajardo-Acosta, S. B., Stencel, R. E., & Backman, D. E. 1998a, ApJL, 503, L193
Fajardo-Acosta, S. B., Telesco, C. M., & Knacke, R. F. 1998b, AJ, 115, 2101
Fang, M., van Boekel, R., Bouwman, J., et al. 2013, A&A, 549, A15
Fedele, D., Bruderer, S., van Dishoeck, E. F., et al. 2013, A&A, 559, A77
Federman, S. R., Glassgold, A. E., Jenkins, E. B., & Shaya, E. J. 1980, ApJ, 242, 545
Feigelson, E. D., Lawson, W. A., & Garmire, G. P. 2003, ApJ, 599, 1207
Folsom, C. P., Bagnulo, S., Wade, G. A., et al. 2012, MNRAS, 422, 2072
Fukui, Y., Onishi, T., Abe, R., et al. 1999, PASJ, 51, 751
Fumel, A., & Böhm, T. 2012, A&A, 540, A108
Garcia, P. J. V., Benisty, M., Dougados, C., et al. 2013, MNRAS, 430, 1839
García-López, R., Natta, A., Testi, L., & Habart, E. 2006, A&A, 459, 837
Gontcharov, G. A. 2007, yCat, 903, 20844
Grady, C. A., Woodgate, B., Torres, C. A. O., et al. 2004, ApJ, 608, 809
Greaves, J. S., Coulson, I. M., & Holland, W. S. 2000, MNRAS, 312, L1
Guilloteau, S., Di Folco, E., Dutrey, A., et al. 2013, A&A, 549, A92
Guilloteau, S., & Lucas, R. 2000, in ASP Conf. Ser. 217, Imaging at Radio through Submillimeter Wavelengths, ed. J. G. Mangum & S. J. E. Radford (San Francisco, CA: ASP), 299
Güsten, R., Baryshev, A., Bell, A., et al. 2008, Proc. SPIE, 7020, 25
Güsten, R., Nyman, L. Å., Schilke, P., et al. 2006, A&A, 454, L13
Hamaguchi, K., Yamauchi, S., & Koyama, K. 2005, ApJ, 618, 360
Hara, A., Tachihara, K., Mizuno, A., et al. 1999, PASJ, 51, 895
Harju, J., Haikala, L. K., Mattila, K., et al. 1993, A&A, 278, 569
Hauck, B., & Mermilliod, M. 1998, A&AS, 129, 431
Henning, T., Launhardt, R., Steinacker, J., & Thamm, E. 1994, A&A, 291, 546
Hillenbrand, L. A., Carpenter, J. M., Kim, J. S., et al. 2008, ApJ, 677, 630
Høg, E., Fabricius, C., Makarov, V. V., et al. 2000, A&A, 355, L27
Hollenbach, D. J., Yorke, H. W., & Johnstone, D. 2000, in Protostars and Planets IV, ed. V. Mannings, A. P. Boss, & S. S. Russell (Tucson, AZ: Univ. Arizona Press), 401
Houk, N. 1978, Michigan Catalogue of Two-dimensional Spectral Types for the HD Stars (Ann Arbor: Dept. Astronomy, Univ. Michigan)
Hu, J. Y., The, P. S., & de Winter, D. 1989, A&A, 208, 213
Hughes, A. M., Andrews, S. M., Wilner, D. J., et al. 2010, AJ, 140, 887
Hughes, A. M., Wilner, D. J., Kamp, I., & Hogerheijde, M. R. 2008a, ApJ, 681, 626
Hughes, A. M., Wilner, D. J., Qi, C., & Hogerheijde, M. R. 2008b, ApJ, 678, 1119
Ingleby, L., Calvet, N., Hernández, J., et al. 2011, AJ, 141, 127
Jonkheid, B., Dullemond, C. P., Hogerheijde, M. R., & van Dishoeck, E. F. 2007, A&A, 463, 203
Juhász, A., Bouwman, J., Henning, T., et al. 2010, ApJ, 721, 431
Kohno, K. 2005, in ASP Conf. Ser. 344, The Cool Universe: Observing Cosmic Dawn, ed. C. Lidman & D. Alloin (San Francisco, CA: ASP), 242
Kóspál, Á., Moór, A., Juhász, A., et al. 2013, ApJ, 776, 77
Kraus, S., Hofmann, K.-H., Benisty, M., et al. 2008, A&A, 489, 1157
Kun, M., Vinkó, J., & Szabados, L. 2000, MNRAS, 319, 777
Kurucz, R. L. 1993, ATLAS9 Stellar Atmosphere Programs and 2 km/s Grid. CD-ROM No. 13 (Cambridge, MA, Smithsonian Astrophysical Observatory)
Lee, H.-H., Bettens, R. P. A., & Herbst, E. 1996, A&AS, 119, 111
Liu, T., Zhang, H., Wu, Y., Qin, S.-L., & Miller, M. 2011, ApJ, 734, 22
Luna, R., Cox, N. L. J., Satorre, M. A., et al. 2008, A&A, 480, 133

Lyo, A.-R., Lawson, W. A., & Bessell, M. S. 2008, MNRAS, 389, 1461
Malfait, K., Bogaert, E., & Waelkens, C. 1998, A&A, 331, 211
Mannings, V., & Barlow, M. J. 1998, ApJ, 497, 330
Martin-Zaïdi, C., Habart, E., Augereau, J.-C., et al. 2009, ApJ, 695, 1302
Martin-Zaïdi, C., van Dishoeck, E. F., Augereau, J.-C., Lagage, P.-O., & Pantin, E. 2008, A&A, 489, 601
Meeus, G., Montesinos, B., Mendigutía, I., et al. 2012, A&A, 544, A78
Meeus, G., Waters, L. B. F. M., Bouwman, J., et al. 2001, A&A, 365, 476
Meyer, M. R., Backman, D. E., Weinberger, A. J., & Wyatt, M. C. 2007, in Protostars and Planets V, ed. B. Reipurth, D. Jewitt, & K. Keil (Tuscon, AZ: Univ. Arizona Press), 573
Mizuno, A., Hayakawa, T., Yamaguchi, N., et al. 1998, ApJL, 507, L83
Mizuno, A., Yamaguchi, R., Tachihara, K., et al. 2001, PASJ, 53, 1071
Moerchen, M. M., Telesco, C. M., & Packham, C. 2010, ApJ, 723, 1418
Montesinos, B., Eiroa, C., Mora, A., & Merín, B. 2009, A&A, 495, 901
Moór, A., Ábrahám, P., Juhász, A., et al. 2011, ApJL, 740, L7
Nyman, L.-A., Booth, R. S., Carlstrom, U., et al. 1992, A&AS, 93, 121
Öberg, K. I., Qi, C., Fogel, J. K. J., et al. 2011, ApJ, 734, 98
Ohashi, N. 2008, Ap&SS, 313, 101
Onishi, T., Kawamura, A., Abe, R., et al. 1999, PASJ, 51, 871
Ortiz, R., Lorenz-Martins, S., Maciel, W. J., & Rangel, E. M. 2005, A&A, 431, 565
Owen, J. E., Clarke, C. J., & Ercolano, B. 2012, MNRAS, 422, 1880
Panić, O., & Hogerheijde, M. R. 2009, A&A, 508, 707
Panić, O., van Dishoeck, E. F., Hogerheijde, M. R., et al. 2010, A&A, 519, A110
Pascucci, I., Gorti, U., Hollenbach, D., et al. 2006, ApJ, 651, 1177
Pavlyuchenkov, Y., Semenov, D., Henning, T., et al. 2007, ApJ, 669, 1262
Pinte, C., Ménard, F., Duchêne, G., & Bastien, P. 2006, A&A, 459, 797
Pollack, J. B., Hubickyj, O., Bodenheimer, P., et al. 1996, Icar, 124, 62
Qi, C., D'Alessio, P., Öberg, K. I., et al. 2011, ApJ, 740, 84
Redfield, S., Kessler-Silacci, J. E., & Cieza, L. A. 2007, ApJ, 661, 944
Rhee, J. H., Song, I., & Zuckerman, B. 2007a, ApJ, 671, 616
Rhee, J. H., Song, I., Zuckerman, B., & McElwain, M. 2007b, ApJ, 660, 1556
Rieke, G. H., Su, K. Y. L., Stansberry, J. A., et al. 2005, ApJ, 620, 1010
Sandell, G., Weintraub, D. A., & Hamidouche, M. 2011, ApJ, 727, 26
Schütz, O., Böhnhardt, H., Pantin, E., et al. 2004, A&A, 424, 613
Schütz, O., Meeus, G., Carmona, A., Juhász, A., & Sterzik, M. F. 2011, A&A, 533, A54
Shimoikura, T., & Dobashi, K. 2011, ApJ, 731, 23
Silverstone, M. D. 2000, PhD thesis, Univ. California
Siringo, G., Kreysa, E., Kovács, A., et al. 2009, A&A, 497, 945
Straižys, V., Černis, K., & Bartasiute, S. 1996, BaltA, 5, 125
Sylvester, R. J., & Mannings, V. 2000, MNRAS, 313, 73
Tachihara, K., Mizuno, A., & Fukui, Y. 2000, ApJ, 528, 817
Takeuchi, T., & Artymowicz, P. 2001, ApJ, 557, 990
Tatulli, E., Isella, A., Natta, A., et al. 2007, A&A, 464, 55
Thé, P. S., de Winter, D., & Perez, M. R. 1994, A&AS, 104, 315
Thi, W. F., van Dishoeck, E. F., Blake, G. A., et al. 2001, ApJ, 561, 1074
van der Plas, G., van den Ancker, M. E., Fedele, D., et al. 2008, A&A, 485, 487
van Kempen, T. A., van Dishoeck, E. F., Brinch, C., & Hogerheijde, M. R. 2007, A&A, 461, 983
van Leeuwen, F. 2007, A&A, 474, 653
Verhoeff, A. P., Min, M., Acke, B., et al. 2010, A&A, 516, A48
Vieira, S. L. A., Corradi, W. J. B., Alencar, S. H. P., et al. 2003, AJ, 126, 2971
Wade, G. A., Bagnulo, S., Drouin, D., Landstreet, J. D., & Monin, D. 2007, MNRAS, 376, 1145
Walker, H. J., & Wolstencroft, R. D. 1988, PASP, 100, 1509
Walsh, C., Millar, T. J., & Nomura, H. 2010, ApJ, 722, 1607
Weidenschilling, S. J. 1977, MNRAS, 180, 57
Williams, J. P., & Cieza, L. A. 2011, ARA&A, 49, 67
Wyatt, M. C. 2008, ARA&A, 46, 339
Wyatt, M. C., Greaves, J. S., Dent, W. R. F., & Coulson, I. M. 2005, ApJ, 620, 492
Wyatt, M. C., Smith, R., Su, K. Y. L., et al. 2007, ApJ, 663, 365
Woitke, P., Kamp, I., & Thi, W.-F. 2009, A&A, 501, 383
Yamamura, I., Makiuti, S., Ikeda, N., et al. 2011, VizieR Online Data Catalog, 2298, 0
Yi, S., Demarque, P., Kim, Y.-Ch., et al. 2001, ApJS, 136, 417
Zagorovsky, K., Brandeker, A., & Wu, Y. 2010, ApJ, 720, 923
Zhang, X., Lee, Y., Bolatto, A., & Stark, A. A. 2001, ApJ, 553, 274
Zuckerman, B. 2001, ARA&A, 39, 549
Zuckerman, B., Forveille, T., & Kastner, J. H. 1995, Natur, 373, 494